



Research paper

Porous medium-based PTO damping and overset mesh motion: A combined approach for effective OpenFOAM[®] simulations of floating OWCs

Gabriel Barajas^{a,*}, Javier L. Lara^a, Josh Davidson^c, Alessandro Romano^{b,a}

^a IHCantabria - Instituto de Hidráulica Ambiental de la Universidad de Cantabria, Calle Isabel Torres 15, Santander 39011, Spain

^b Roma Tre University, Department of Civil, Computer Science and Aeronautical Technologies Engineering, Rome 00146, Italy

^c BCAM - Basque Center for Applied Mathematics, Mazarredo Zumarkalea 14, Bilbao 48009, Spain



ARTICLE INFO

Keywords:

CFD
OpenFOAM
WEC
PTO
Overset mesh method
Water waves

ABSTRACT

This paper introduces a robust framework within the OpenFOAM[®] environment to model the complex case of floating Oscillating Water Column (OWC) systems. It integrates existing modules for wave generation and absorption, overset mesh for dynamic mesh motion, and the Moody mooring model. A significant novel contribution of this work is the incorporation of a movable porous medium zone, designed to emulate the damping effect of the Power Take-Off (PTO) turbine. The paper first presents a validation of the coupled framework, comprising the tailored version of the two-phase fluid dynamics solver with the porous medium zones, the Overset algorithm for mesh motion and the Moody model for mooring systems. The validated model is then used to demonstrate the capabilities of the porous media zone in replicating the PTO damping for a floating OWC under constant loadings and regular waves. It is observed that the presence of the PTO alters the natural frequency and maximum displacements of the floating body, but has very little influence in the main displacements. The different characterisations of the PTO influence the frictional forces. The air flow is modified in the vicinity of the PTO due to the frictional forces exerted by the porous zone.

1. Introduction

The quest for sustainable and renewable energy sources has led to significant advancements in offshore renewable energy technologies, among which Oscillating Water Columns (OWCs) have emerged as a promising solution for wave energy conversion. The concept of OWCs, extensively reviewed in [Falcão and Henriques \(2016\)](#), has evolved considerably since its inception. While many OWC designs are fixed structures, anchored to the seabed or integrated into breakwaters, floating OWCs distinguish themselves through their versatility and wide range of applications. Beyond their primary role in wave energy conversion, floating OWCs are also deployed in diverse applications such as powering oceanographic equipment ([Mathias et al., 2021](#); [Oikonomou et al., 2021](#); [Korde et al., 2024](#)), supporting marine-based wireless sensor networks ([Chowdhury et al., 2015](#); [Henriques et al., 2016](#); [Du et al., 2021](#)), and even acting as a stabilising mechanism for floating platforms ([Crema et al., 2015](#); [Howe, 2020](#); [de Oliveira Costa et al., 2023](#)). This innovative approach, dates back to the pioneering work of Masuda in the 1940s ([Masuda, 1986](#)), originally aimed at powering navigational buoys. Recent concepts have explored the integration of floating OWCs with offshore wind turbines, aiming to enhance power output, reduce variability, and stabilise the motion of

floating structures ([Zhu et al., 2020](#); [M'zoughi et al., 2021](#); [Zhou et al., 2023](#)).

Although promising, floating OWCs are currently at various stages of technological readiness levels (TRLs), ranging from conceptual designs and laboratory prototypes to more advanced pilot installations. While some applications, such as powering navigational buoys, have reached high TRLs, integrating this technology for other applications remains at lower TRLs. The multifaceted applications and evolving designs of floating OWCs highlight their significance in the field of ocean engineering and the need for advanced research and optimisation to fully harness their potential, particularly as they transition from experimental stages to commercial viability.

1.1. Computational fluid dynamics simulations of OWCs

Computational Fluid Dynamics (CFD) simulations of OWCs have become increasingly vital, particularly at the lower TRLs. These early stages of development are pivotal for improving the techno-economic aspects of device concepts, where extensive numerical modelling enables fast, cost-effective optimisation and refinement, as emphasised

* Corresponding author.

E-mail address: gabriel.barajas@unican.es (G. Barajas).

in Weber (2012). Traditionally, modelling of OWC systems relied heavily on physical scale model testing and simplified theoretical models. This approach was necessitated by the complex nonlinear hydrodynamics of OWCs, which were challenging to capture accurately through basic modelling techniques. The review in Zabala et al. (2019) provides an in-depth analysis of the modelling advancements in the wave-induced fluid effects on floating OWCs. CFD simulations are primarily applied in TRLs 3 to 5, aiding in the proof-of-concept, design optimisation, and validation of components in relevant environments. For example, Zabala et al. (2019) propose a four-step industrial methodology for the development of floating OWCs, where CFD simulations are the key component in Steps 2 and 3 to develop a “digital prototype”.

Physical scale model testing, despite offering valuable insights into real fluid–structure interactions, presents significant limitations. Performing experiments in wave tank facilities is not only expensive but also limited in its ability to rapidly refine and optimise prototype geometries. Furthermore, the compressibility of the air chamber within OWCs does not scale down in the same manner as other system components, introducing discrepancies in the model’s accuracy (Viviano et al., 2018; Falcão et al., 2022). On the other hand, simplified theoretical models, while useful for basic understanding, fall short in their capability to encapsulate the complex fluid–structure interactions and the nonlinear hydrodynamic phenomena inherent in OWC systems. These shortcomings underscore the need for more advanced and comprehensive modelling techniques.

The introduction of CFD into the realm of OWC modelling has been transformative. With the growth in computational capabilities, CFD has emerged as a powerful tool that can effectively capture the complexities of OWC systems. Two-phase CFD simulations, in particular, have enabled the simultaneous analysis of hydrodynamic wave-structure interactions (Palm et al., 2016; Wang and Zhang, 2021; Zhou et al., 2021a; Pinguet et al., 2022; Chen and Hall, 2022; Masoomi et al., 2023; Chen et al., 2024; Khan et al., 2024) and the aerodynamic aspects within the OWC chamber (Iturriz et al., 2015; Gadelho et al., 2022). This high-fidelity simulation environment, though computationally intensive, provides detailed insights into the fluid dynamics and pressures within the system, which are critical for optimising energy conversion efficiency and understanding the OWC’s operational behaviour in various sea conditions. Recent reviews, such as Windt et al. (2018) and Opoku et al. (2023), showcase the progressive use of CFD in understanding and enhancing OWC performance.

1.2. Modelling the damping effect of the PTO within the CFD simulation

Accurately representing the damping effect of the PTO mechanism is essential for realistic and effective simulation of wave energy conversion. The PTO’s role in inducing pressure changes within the OWC’s air column directly influences the efficiency of energy extraction. Various approaches have been adopted to replicate the damping effects of the PTO in CFD simulations, each with its specific application and level of detail.

The commonly accepted practice for representing the PTO mechanism involves two primary methods: using an orifice model or employing porous media. The choice between these methods is often dictated by the type of PTO device being simulated. Orifice models are typically used to simulate nonlinear PTO devices, such as Impulse turbines, as they replicate the high-pressure drops across small orifice plates, a method aligned with physical experiments. In contrast, porous media are used to represent linear PTO devices like Wells turbines, which rely on a more gradual pressure drop mechanism. This approach mirrors physical experiments where filter membranes are used to simulate the pressure drop across the PTO. The utilisation of these methods is grounded in their ability to closely mimic real-world PTO characteristics and their effectiveness in scaled experiments, as noted by Sarmiento (1992).

Another method, less commonly used in the context of OWCs but prevalent in applications such as wind turbines, is the Actuator Disk Model (ADM). ADM offers a simplified representation of the energy extraction process by introducing a momentum sink in the flow, thereby simulating the damping effect of the PTO. However, only a few studies explore this approach (Moñino et al., 2017; Medina-Lopez et al., 2019). This might be due to ADM’s inherent simplification, which, while efficient and less computationally demanding, may not capture the detailed fluid dynamics and specific characteristics of PTO mechanisms in OWC systems as accurately as the orifice or porous media models.

Table 1 provides a summary comparison of these three approaches, highlighting their respective strengths and weaknesses in the context of PTO modelling in OWC systems. From this comparison the porous media emerges as an attractive option. An early attempt at replicating a porous media PTO used in experiments, positioned the top of a cylindrical OWC at the atmospheric boundary in the CFD simulation and imposed a boundary condition comprising a linear law relating the pressure drop to the mass flow rate to take into account the presence of the porous membrane (Didier and Paixão Conde, 2011). In two-dimensional simulations, Kamath et al. (2015a,b) accounted for PTO damping by introducing a linear pressure drop at the OWC vent, deriving the permeability coefficient from Darcy’s law for flow through porous media. Similarly, Scarpetta et al. (2017) and Gurnari et al. (2020, 2022) incorporated a porous media zone, characterised by viscous and inertial losses, into the exhaust outlet of a 2D U-OWC. Other studies focusing on 2D onshore OWCs include Güths et al. (2022). Advancing to three-dimensional models, Gadelho et al. (2022) compared results against experimental data using three different methods for simulating PTO damping: (1) directly replicating the physical holes used in experiments, (2) applying a velocity damping term, and (3) employing porous media. They found that while all methods yielded similar accuracy, methods (2) and (3) offered considerable computational speed-ups. Most recently, Didier and Teixeira (2024) examined an array of OWCs integrated into a vertical breakwater wall, utilising a porous media zone to replicate the PTO damping effect. While these studies have demonstrated that including a porous media zone to represent PTO damping in CFD simulations of OWCs is an accurate and reliable approach – validated against experimental data – they all consider fixed OWC structures. To date, the integration of porous media to represent PTO damping in floating OWCs has not been investigated.

1.3. Challenges in floating OWC simulation

Simulating floating OWCs presents a unique set of computational challenges, distinct from those encountered with fixed OWCs. These challenges primarily arise from the inherent large amplitude displacements typical of wave-driven floating structures, coupled with the complexity of accurately modelling mooring systems. Despite the progress in this field, the review by Windt et al. (2018) highlights a significant gap in the literature, with only 5 out of 65 publications on CFD simulations of OWCs considering floating OWCs. This emphasises the need for more focused research in this area, leveraging the capabilities of advanced CFD tools to address the unique challenges posed by floating OWC systems.

The mathematical modelling of mooring systems for WECs, as reviewed by Davidson and Ringwood (2017), is integral to these simulations. For example, the influence of mooring systems on the power production of floating OWCs is investigated by Gubesch et al. (2022). The integration of sophisticated mooring models like Moody and MorDyn within the OpenFOAM framework, as explored in the studies by Palm et al. (2016) and Chen and Hall (2022), underscores the complexity inherent in accurately simulating these systems.

A significant challenge in CFD modelling of floating OWCs is the management of mesh motion-capable of handling the range of wave

Table 1
Comparison of the different approaches to modelling the PTO in an OWC.

Model	Strengths	Weaknesses
Orifice	• Directly replicates physical experiments using orifices. • Suitable for detailed analysis of flow through small openings.	• Requires new geometry and mesh for different damping values. • High velocities through small orifices necessitate fine meshes and small time-steps, increasing computational time.
ADM	• Efficiently simulates energy extraction without detailed geometric modelling. • Less computationally intensive. • Useful for generalised studies of PTO effects.	• May oversimplify the damping effect and PTO mechanics. • Less accurate in capturing complex fluid-PTO interactions.
Porous media	• Accurately represents pressure drop and damping effects in the PTO zone without detailed geometric modelling. • Avoids the need for extremely fine meshes, balancing detail and computational efficiency. • Adaptable for various PTO types including linear and nonlinear devices.	• Adds complexity with additional terms and parameters in the simulation. • More computationally demanding than ADM, requiring careful calibration and validation.

and current driven displacements of the OWC structure. Several techniques have been developed, each offering unique benefits and constraints. Mesh morphing, sliding interfaces, overset mesh, cut cell and immersed boundary methods are some of the notable options in this domain. The works of [Constant et al. \(2017\)](#), [Davidson et al. \(2019\)](#) and [Palm and Eskilsson \(2022\)](#) delve into these techniques, offering insights into their applicability and effectiveness in different scenarios. The choice of the appropriate mesh motion technique is crucial, as it directly impacts the accuracy and efficiency of the simulations, thereby influencing the overall reliability of the CFD model in capturing the complex dynamics of floating OWCs. This aspect of CFD modelling, therefore, represents a critical area of focus for effective simulation of floating OWCs.

1.4. Objectives and outline of paper

This paper presents a comprehensive and robust CFD framework tailored to the complex requirements of floating OWCs, addressing hydrodynamics, fluid–structure interaction, body motion, air dynamics, mesh motion, mooring systems, and PTO mechanisms. Our framework integrates modules for wave generation and absorption, implements dynamic mesh motion using the overset mesh method, all coupled with the Moody mooring model, offering a sophisticated toolset for simulating floating OWC systems. A key novelty of this work is the representation of the PTO as a porous medium zone implemented within the overset framework. This enables the PTO to move in unison with the floating structure, a capability critically lacking for floating OWCs.

This paper focuses on the use of OpenFOAM, an open-source C++ toolbox for developing customised numerical solvers and utilities. OpenFOAM's versatility is evident in its application to OWC-WECs, where PTOs are often modelled as orifices. Studies such as those by [Iturrioz et al. \(2015\)](#), [Simonetti et al. \(2017\)](#) and [Xu and Huang \(2019\)](#) have validated and utilised OpenFOAM for various aspects of OWC-WEC analysis. Several software tools, based on diverse numerical methods, are available for simulating OWC interactions with waves. These are cataloged, with their varying strengths and weaknesses in the review of CFD for OWCs in [Opoku et al. \(2023\)](#), showing the ANSYS FLUENT is the most popularly used tool with 37% of the reviewed publications and OpenFOAM coming in second with 20%. Interestingly, a broader review of all types of WECs by [Windt et al. \(2018\)](#) shows a reversal in these roles, with OpenFOAM leading at 39% and FLUENT at 20%. This perhaps indicates the requirement for improvement in OpenFOAM's capabilities specifically for OWC simulations, a gap this paper aims to address.

The structure of the paper is organised as follows:

- Section 2 elaborates on the governing equations and details the innovative numerical implementation of the porous medium within the overset mesh framework for simulating the PTO in a floating OWC.

- Section 3 presents a comprehensive validation of our approach against experimental data and numerical benchmarks, including both free and moored decay tests, as well as interactions with regular waves.
- Section 4 applies the validated model to parametric simulations, examining decay tests, interactions with constant currents and regular waves, emphasising the effectiveness of the porous medium approach.
- Section 5 concludes the paper, summarising key findings and discussing their implications for future research in floating OWC systems and offshore renewable energy technologies.

2. Numerical model

This study builds upon the IHFOAM suite of tools ([Higuera et al., 2013](#); [Di Paolo et al., 2021a,b](#)), which is integrated into the open-source OpenFOAM platform ([ESI-Group, 2021](#); [Jasak, 1996](#)). IHFOAM is specifically tailored for coastal and offshore engineering applications, featuring advanced boundary conditions for wave and current generation and absorption, as well as solvers for porous media ([Romano et al., 2020](#)). The suite is capable of solving both three-dimensional Reynolds Averaged Navier–Stokes (RANS) equations and Volume Averaged Reynolds Averaged Navier–Stokes (VARANS) equations ([Higuera et al., 2013](#)), catering to two-phase flow scenarios. Additionally, the Overset mesh technique is employed to capture the floating OWC body motion, alongside the integration of the external Moody library ([Palm et al., 2017](#)) to model the mooring systems.

2.1. Governing equations

This study employs two sets of equations (RANS and VARANS) to accurately describe the fluid dynamics within the simulation domain. The RANS equations, which govern the fluid behaviour in most of the domain, are detailed in Section 2.1.1. In contrast, within the PTO zone, where porous media are utilised to replicate damping effects, the VARANS equations are applied as elaborated in Section 2.1.2. The implementation of these governing equations within the OpenFOAM framework is subsequently described in Section 2.1.3.

2.1.1. The main fluid domain

The fluid dynamics in the main domain (no PTO is defined) are governed by the RANS equations, which encompass the conservation of mass and momentum (to model the fluid flow), coupled with the Volume of Fluid (VoF) equation (to model the interface between water and air). These equations are represented as follows:

$$\frac{\partial u_i}{\partial x_i} = 0 \quad (1)$$

$$\frac{\partial \rho u_i}{\partial t} + u_j \frac{\partial \rho u_i}{\partial x_j} = -g_j x_j \frac{\partial \rho}{\partial x_i} - \frac{\partial p^*}{\partial x_i} - f_{\sigma i} - \frac{\partial}{\partial x_j} \mu_{\text{eff}} \left(\frac{\partial \rho u_i}{\partial x_j} + \frac{\partial \rho u_j}{\partial x_i} \right) \quad (2)$$

$$\frac{\partial \alpha}{\partial t} + \frac{\partial u_i \alpha}{\partial x_i} + \frac{\partial u_{ci} \alpha (1 - \alpha)}{\partial x_i} = 0 \quad (3)$$

where u_i [m/s] are the ensemble averaged components of the velocity, x_i [m] the Cartesian coordinates, g_j [m/s²] the components of the gravitational acceleration, ρ [kg/m³] the density of the fluid, p^* [Pa] the ensemble averaged pressure in excess of hydrostatic, α [-] the volume fraction (VoF), $f_{\sigma i}$ [N/m³] the surface tension, μ_{eff} [Pa s] is the effective dynamic viscosity that is defined as $\mu_{\text{eff}} = \mu + \rho \nu_i$ and takes into account the dynamic molecular (μ) and the turbulent viscosity effects ($\rho \nu_i$). u_{ci} is the compression velocity [m/s].

2.1.2. The PTO region

The VARANS equations are employed to model the flow in the PTO zone that accounts for the frictional forces exerted by a porous media. The mass and momentum conservation equations (to model the fluid flow), coupled to the VoF equation (to model the interface between water and air), are expressed as follows:

$$\frac{\partial}{\partial x_i} \frac{\bar{u}_i}{n} = 0 \quad (4)$$

$$(1+c) \frac{\partial}{\partial t} \frac{\rho \bar{u}_i}{n} + \frac{\bar{u}_j}{n} \frac{\partial}{\partial x_j} \frac{\rho \bar{u}_i}{n} = -g_j x_j \frac{\partial \rho}{\partial x_i} - \frac{\partial \bar{p}^*}{\partial x_i} - f_{\sigma i} - \frac{\partial}{\partial x_j} \mu_{\text{eff}} \left(\frac{\partial}{\partial x_j} \frac{\rho \bar{u}_i}{n} + \frac{\partial}{\partial x_i} \frac{\rho \bar{u}_j}{n} \right) - A \bar{u}_i - B |\bar{u}_i| \bar{u}_i \quad (5)$$

$$\frac{\partial \alpha}{\partial t} + \frac{\partial \bar{u}_i \alpha}{\partial x_i} + \frac{\partial \bar{u}_{ci} \alpha (1 - \alpha)}{\partial x_i} = 0 \quad (6)$$

where \bar{u}_i [m/s] are the volume averaged ensemble averaged velocity components, \bar{p}^* [Pa] the volume averaged ensemble averaged pressure in excess of hydrostatic, α [-] the volume fraction (VoF), n [-] is the porosity, g_j [m/s²] the components of the gravitational acceleration, ρ [kg/m³] the density of the fluid, $f_{\sigma i}$ [N/m³] the surface tension and μ_{eff} [Pa s] is the effective dynamic viscosity that is defined as $\mu_{\text{eff}} = \mu + \rho \nu_i$ and takes into account the dynamic molecular (μ) and the turbulent viscosity effects ($\rho \nu_i$). u_{ci} is the compression velocity [m/s]. Van Gent (1995) describes the coefficient A [-] to take into account the frictional force induced by laminar Darcy-type flow, the coefficient B [-] to take into account the frictional force induced under turbulent flow conditions and the coefficient c [-] to take into account the added mass in a set of equations. These equations are represented as follows:

$$A = a \frac{(1-n)^2}{n^3} \frac{\mu}{D_{50}^2}, \quad (7)$$

$$B = b \left(1 + \frac{7.5}{KC} \right) \frac{(1-n)}{n^3} \frac{\rho}{D_{50}}, \quad (8)$$

$$c = \gamma \frac{1-n}{n} \quad (9)$$

where a [-] is an empirical non-dimensional coefficients, b [-] is an empirical non-dimensional coefficients (see Lara et al., 2011; Losada et al., 2016) and $\gamma = 0.34$ [-] is a non dimensional parameter as proposed by Van Gent (1995). D_{50} [m] is the mean nominal diameter of the porous material, ρ [(kg/m³)] the density of the fluid and μ [Pa s] is the dynamic molecular viscosity and KC [-] the Keulegan–Carpenter number which introduces additional friction due to the oscillatory nature and unsteadiness of the system, defined as follows:

$$KC = \frac{uT}{D_{50}n} \quad (10)$$

where u [m/s] is the amplitude of the flow velocity oscillation (or the amplitude of the object's velocity, in case of an oscillating object), T [s] is the period of the oscillation. D_{50} [m] is the mean nominal diameter of the porous material and n [-] is the porosity. In the present work, following the work by Dong et al. (2024), in order to avoid a situation in which the flow velocity equals to zero that might lead to infinite KC values, we have neglected the variation of B with respect to KC . For the simulations presented in this paper, following the pragmatic approach

by Jacobsen et al. (2017), the additional resistance in the case of an oscillatory wave motion values 1.1. The porous media formulation used in this work is normally used for characterising permeable structures such breakwaters, and it has been formulated and validated in Higuera et al. (2014) against experimental data (Lin, 1998; Guanche et al., 2009; Lara et al., 2012.). The VARANS equations were extended to the overset framework and validated by Romano et al. (2020) against experimental data (Liu et al., 2005). Finally, the VARANS equations have been applied to model the PTO damping on the performance of an onshore dual chamber OWC, being validated (Gadelho et al., 2022) against experimental data that was performed at the COI3 irregular wave flume located at the National Laboratory of Civil Engineering (LNEC), Portugal.

2.1.3. Implementation

The implementation of these equations in the OpenFOAM framework, as described by Romano et al. (2020), is encapsulated in a bespoke solver that works as follows: in regions of clear fluid (outside the porous zone), the frictional forces exerted by the porous media are negated ($a = b = c = 0$), and the porosity n is set to 1, effectively replacing VARANS with RANS. Conversely, within the porous region, the empirical coefficients, parameters, and porosity related to the porous media (i.e., a , b , c , D_{50} , KC , and n) are defined, enabling the full set of VARANS to be solved. The solver supports various turbulence models, including two-equation models like $k-\epsilon$, $k-\omega$, and $k-\omega$ -SST. For this study, the $k-\omega$ -SST turbulence model is employed, enhanced as per Larsen and Fuhrman (Larsen and Fuhrman, 2018) to limit turbulence overproduction.

2.2. Additional components

This section delves into the additional numerical components integral to the simulation's functionality. These components, namely the Mesh Motion and the Mooring Model, play pivotal roles in accurately capturing the dynamics of the floating body and its interaction with the surrounding environment. Each component's implementation within the framework is detailed, highlighting their individual contributions to the overall simulation accuracy and efficiency.

Fig. 1 provides a flow chart to explain the coupling between the motion solver (overset) and the fluid solver (VARANS equations). At every time step, first the motion of the WEC and afterwards of the mesh is solved. Next, the fluid motion is solved. Initially the total acceleration and forces acting on the body are updated to calculate the new position of the WEC (*sixDoFRigidBodyMotion* library, Section 2.2.1), imposing the restraints of the mooring (*Moody* library, Section 2.2.2). Only the contributions from the fluids and the moorings are taken into account. The effects of the PTO damping, imposing a resistance to the air flow, are simulated by means of porous material that exerts a resistance in the air circulation, modifying the fluids flow inside the chamber of the WEC. Then, the mesh is moved where the new position of the WEC is used as the boundary condition (*overset* framework). Once the mesh is moved to the new position, the fluid solver is started. The position of the free surface (VoF) is calculated (by means of the algorithm *MULES*) and the turbulent viscosity effects are updated (*kOmegaSST* turbulence model). Then, the *PIMPLE* algorithm is used to solve the VARANS equations (momentum and pressure equations) to calculate the velocity field and the pressure field. This process is repeated for all time steps.

2.2.1. Body motion

In the present study, the motion of the body is defined by six degrees of freedom (6-DoF), heave, sway, surge, pitch, roll and yaw, and it is calculated using the 6-DoF motion library, named *sixDoFRigidBodyMotion*.

To accommodate the motion of the floating OWC within the computational domain, the overset mesh method is employed. The Overset mesh technique, as detailed in Romano et al. (2020), forms the cornerstone

of our simulation's ability to handle complex geometries and large displacements. This technique employs two distinct domains: a moving domain, which accounts for the displacements of the floating body, and a background domain, representing the numerical wave tank (NWT). The integration of these domains results in a new, overlapped mesh that not only accommodates complex shapes and significant movements but also maintains high mesh quality, essential for accurate simulations. Previous research (Pinguet et al., 2022; Katsidoniotaki and Götteman, 2022; Chen and Hall, 2022; Chen et al., 2024; Khan et al., 2024) has demonstrated that the overset mesh technique is an accurate and reliable framework for simulating interactions between waves and floating devices. Building upon this foundation, our study extends the proven usefulness of the overset approach by integrating a porous medium into the overset framework—a crucial advancement that enables the porous media region to serve as the PTO zone for a floating OWC. This integration allows the PTO zone to precisely translate and rotate with the floating body, ensuring it remains in its required position at the exit of the OWC chamber.

2.2.2. Mooring model

In simulating the dynamic behaviour of mooring cables within the OpenFOAM framework, two advanced mooring models implemented in C++ are commonly used: *MoorDyn* and *Moody*. Both models include axial stiffness, internal damping, line weight, buoyancy, seabed contact, drag and inertia forces and ignore torsion. *MoorDyn* is a lumped mass model and *Moody* is a finite-element model. The main differences are that *MoorDyn* is capable of including bending stiffness but does not calculate fluid forces due to currents and waves acting directly on the lines (only considers the motion of the lines and not the relative motion between the fluid and line). In contrast, *Moody* does not include bending stiffness but does compute drag and inertia forces due to currents and waves acting directly on the mooring lines. In addition, the finite-element approach of *Moody* allows it to capture high-frequency dynamics such as snap loads. For the dynamic simulation of mooring cables in this study, we have chosen the *Moody* library, favouring its ability to compute drag and inertia forces due to currents and waves acting and its ability to capture snap loads, whereas its inability to include bending effects are considered less critical for the scenarios investigated in this study.

The *Moody* library is implemented as an hp-adaptive cable solver using the discontinuous Galerkin method, is specifically designed for computing the intricate dynamics of mooring cables. The coupling of OpenFOAM with *Moody* within the overset framework is a critical aspect of the model, ensuring that the mooring system's behaviour is accurately captured. The numerical implementation and validation of *Moody*, as described in Palm et al. (2017), underscore its efficacy in simulating the complex interactions between the mooring cables and the floating body. Previous research (Palm et al., 2016, 2017; Palm and Eskilsson, 2022; Chen and Hall, 2022; Chen et al., 2024; Khan et al., 2024) prove that *Moody* library is an accurate and reliable tool for computing cable dynamics.

2.3. Strengths and limitations

The developed numerical framework exhibits several significant strengths that contribute to advancing the simulation of floating OWC systems. A primary advantage is the use of open-source and freely available software packages, specifically the OpenFOAM platform. This choice enhances accessibility and allows other researchers and practitioners in the community to implement, verify, and build upon the work presented. OpenFOAM's extensive validation and widespread adoption in ocean engineering applications (Huang et al., 2022) underscore the reliability and robustness of the simulations conducted within this study.

A notable innovation in this framework is the incorporation of a movable porous medium zone within the overset mesh framework to

model the PTO damping effects. This approach represents a significant advancement, as it allows the PTO region to move in unison with the floating body, accurately capturing the dynamic interactions between the PTO and the oscillating water column. This capability is critically important for floating OWCs and has been lacking in previous simulation studies. The use of the VARANS equations to parameterise the porous media provides flexibility in modelling different PTO configurations and damping characteristics, enabling comprehensive analysis and optimisation of PTO designs.

The overset mesh motion framework is another strength, offering a reliable and effective means of handling large and complex displacements of floating devices. Traditional mesh morphing strategies can struggle with maintaining mesh quality during significant movements, leading to numerical inaccuracies. In contrast, the overset method maintains high-quality meshes throughout the simulation, ensuring accurate representation of the physical phenomena. Embedding the PTO region within this framework ensures that it remains correctly positioned relative to the floating body, which is essential for simulating the coupled dynamics of the system.

Furthermore, the integration of the *Moody* mooring model enhances the framework's capability to simulate realistic mooring line dynamics under various loading conditions. The finite-element approach of *Moody*, implemented in C++, allows for efficient and detailed simulation of mooring lines, including axial stiffness, internal damping forces, line weight, buoyancy, seabed contact, drag and inertia forces due to current and wave loading on the mooring lines. Additionally, *Moody* is adept at capturing high-frequency dynamics, such as snap loads, which are critical for understanding the full range of mooring line behaviours under extreme conditions.

Despite these strengths, the framework has certain limitations that should be considered. One of the primary drawbacks is the computational cost associated with the overset mesh method. The need to solve complex interpolation and coupling between overlapping meshes significantly increases computational demands. This can make simulations of long-duration events or large computational domains challenging, potentially limiting the practical applicability of the method for extensive parametric studies.

PTO resistance is modelled as a porous media zone that introduces resistance to the airflow within the OWC chamber, effectively simulating the damping effect of the PTO. In our simulation, the damping effect introduced by the porous media alters the pressure distribution and airflow within the OWC chamber, as the VARANS equations can reproduce the resistance effects, imposing a flow resistance inside the porous zone but also reflecting part of the flow that is directed to the walls and to the free-surface elevation. These changes in the internal fluid dynamics generate pressure forces on the internal surfaces of the OWC structure (which are naturally transmitted to the floating body through the fluid–structure interaction) and pressure force in the free-surface elevation inside the chamber. As a result, the PTO's influence on the floating body's motion is indirectly captured by the changes in the fluid forces acting on the structure. Our approach is consistent with other common methods used in CFD simulations of OWCs. For instance, when using an orifice model to simulate the PTO, the pressure drop across the orifice introduces resistance to the airflow, but the resulting forces are not typically calculated and applied directly to the rigid body motion solver. Instead, the effect of the PTO is accounted for indirectly through the modification of the pressure and velocity fields within the fluid domain. While this approach may not explicitly calculate and apply the PTO forces to the rigid body solver, it effectively captures the essential physics of how the PTO affects the floating OWC. The interaction between the modified airflow (due to the porous media) and the structure results in a damping effect on the body's motion, which is observed in our simulation results.

The VARANS parameterisation, while offering flexibility, introduces another limitation due to the need for calibration of empirical coefficients (parameters a , b , and c in the porous media equations). These

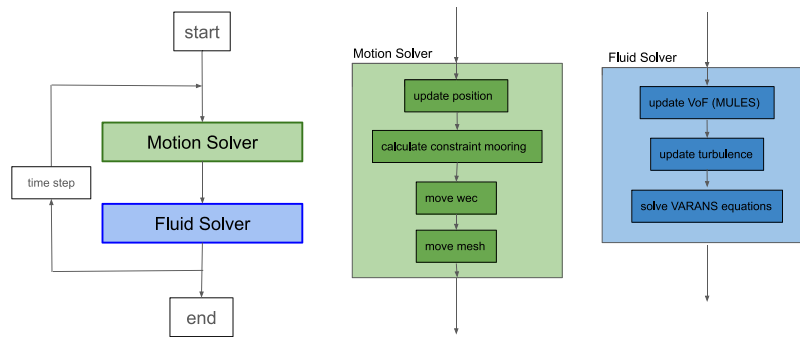


Fig. 1. Flow chart of the numerical solver used to model a WEC with a PTO. Motion of the WEC and mesh algorithm in green, fluid motion algorithm in blue.

coefficients are specific to each application and may require experimental data or detailed empirical studies to determine accurately. This calibration process can be time-consuming and may reduce the generality of the model when applied to different PTO designs or operational conditions.

The porous media approach to modelling the PTO also simplifies the complex geometry and flow dynamics within the PTO region. While this method effectively represents the damping effect, it may not capture detailed fluid–structure interactions, such as turbulent flow patterns and pressure fluctuations caused by turbine blades. Moreover, the current model does not account for air compressibility effects within the OWC chamber, which can be important for accurately predicting the pneumatic performance and energy conversion efficiency of the system.

Additionally, the Moody mooring model does not account for bending and torsional effects in the mooring lines. Therefore, in scenarios where bending and torsional effects are critical, the use of Moody might be a limitation.

In summary, the presented framework offers a robust and innovative approach to simulating floating OWCs with integrated PTO damping effects, leveraging open-source tools and advanced numerical methods. It addresses critical challenges in modelling the coupled dynamics of the floating body, PTO, and mooring system. However, users should be aware of the computational demands and the need for careful calibration of empirical parameters.

3. Model validation

The numerical model is validated to ensure the implementation of the solver, the additional components and their coupling works as expected. The validation case is first described in Section 3.1. The numerical setup is detailed in Section 3.3. In Section 3.4 a grid analysis is carried out. The results are then presented in Section 3.5, which encompass three distinct test scenarios: (1) free decay of an unmoored WEC, (2) free decay of a moored WEC and (3) regular waves interaction with a moored WEC.

3.1. Validation cases

The case study selected to validate the numerical model is a replication of the validation cases presented in Palm et al. (2016), considering a moored floating WEC. The model validated in Palm et al. (2016) shares several similarities to the present numerical model, including the use of OpenFOAM for CFD simulations and the integration of the Moody mooring model. The key differences between the models is that Palm et al. (2016) employ the traditional *interFOAM* solver and use the standard mesh morphing technique to handle the mesh motion, whereas the present numerical model employs our bespoke solver and uses the overset mesh technique for the mesh motion. For validation, we have focused on free-surface elevation in the vicinity of the WEC

Table 2

Catalogue of different test cases simulated. Cases without PTO: *UT*[1,2], *MT*[1,2,3] and *MRM*[1,2], all taken from (Palm et al., 2016). Cases with PTO: *MTPW*, *MTP*, *MTPC* and *MTPW*. δ is initial offset [°] or [m], H is wave target [m], w is the width, T is period [s], n is porosity [–] and U_c is current velocity [m/s].

Test	PTO	Description
Unmoored, decay test 1 (UT1)	No	Heave decay test. $\delta = 0.075$ m
Unmoored, decay test 2 (UT2)	No	Pitch decay test. $\delta = 9.898^\circ$.
Moored, decay test 1 (MT1)	No	surge decay test. $\delta = 0.114$ m
Moored, decay test 2 (MT2)	No	Heave decay test. $\delta = 0.076$ m
Moored, decay test 3 (MT3)	No	Pitch decay test. $\delta = 11.353^\circ$.
Moored, regular waves 1 (MRW1)	No	<i>5/h</i> Stokes theory. $H = 0.04$ m $T = [1.0, 1.2, 1.4]$ s.
Moored, regular waves 2 (MRW2)	No	<i>5/h</i> Stokes theory. $H = 0.08$ m $T = [1.0, 1.2, 1.4]$ s.
Moored, decay test, WEC with PTO (MTPW)	Yes	Heave decay test. $\delta = 0.075$ m $w = [0.08, 0.03, 0.115]$ m
Moored, decay test, WEC with PTO (MTP)	Yes	Heave decay test. $\delta = 0.075$ m $n = [0.05, 0.25, 0.50, 0.75, 1.00]$.
Moored, constant currents, WEC with PTO (MTPC)	Yes	$U_c = [0.25, 0.50, 0.75, 1.0]$ m/s. $n = [0.25, 0.50, 0.75, 1.00]$
Moored, regular waves, WEC with PTO (MTPW)	Yes	<i>5/h</i> Stokes theory. $H = 0.2$ m, $T = 3.0$ s. $n = [0.25, 0.50, 0.75, 1.00]$.

and the WEC's main displacements As depicted in Fig. 1, the mooring forces are calculated and imposed in the rigid body motion equations, the mesh is updated, and then the fluid is solved, with this process repeated at each time step. Therefore, all the different constraints, including the mooring forces, need to be correctly calibrated as the simulation behaves as a unified system. Since we obtain good agreement with the body motions reported by Palm et al. (2016), who thoroughly validated the mooring tensions, we infer that the mooring model is performing accurately in our simulations. Tensions in the mooring lines have not been analysed explicitly; this is a limitation of the present work. Nevertheless, we have included a comparison of the experimental

Table 3
Numerical grids used in the mesh sensibility analysis.

Mesh name	Overset discretisation	Background discretisation	Number of cells
Mesh1 (M1)	$dx = 0.062$ m, $dy = 0.062$ m, $dz = 0.062$ m	$dx = 0.125$ m, $dy = 0.125$ m, $dz = 0.125$ m	0.57M
Mesh2 (M2)	$dx = 0.031$ m, $dy = 0.031$ m, $dz = 0.031$ m	$dx = 0.031$ m, $dy = 0.031$ m, $dz = 0.031$ m	4.32M
Mesh3 (M3)	$dx = 0.015$ m, $dy = 0.015$ m, $dz = 0.015$ m	$dx = 0.031$ m, $dy = 0.031$ m, $dz = 0.015$ m	16.95M

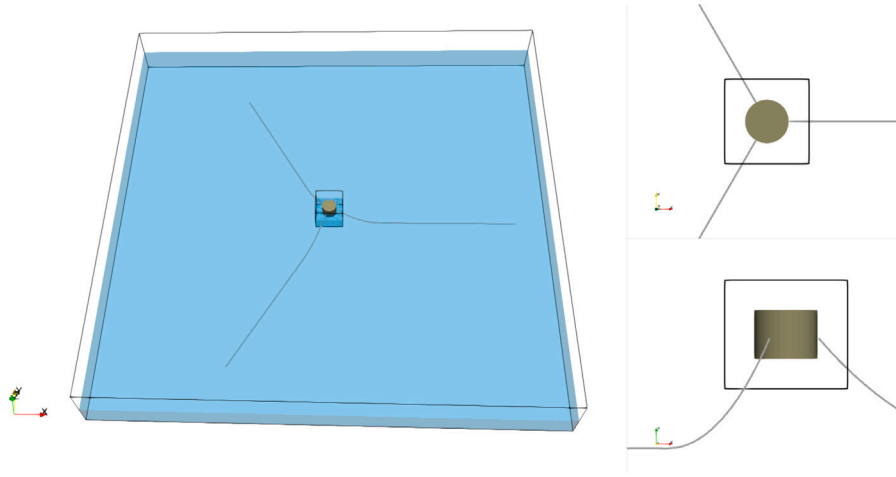


Fig. 2. Left panel, NWT used to validate (Palm et al., 2017), 8 m long, 8 m wide, 2 m high. Initial water level is 0.9 m. The WEC is defined as a cylinder with a diameter $D = 0.515$ m and height $h = 0.4$ m. Background domain and overset domain depicted as black lines, catenaries depicted as grey lines; Right-top panel, plane XY ($z = 1.0$ m), WEC and catenaries; Right-bottom panel, plane XZ ($y = 4$ m), WEC and catenaries.

and numerical tensions of two representative cases to support this assertion.

3.2. Numerical wave tank

The floating WEC is the same cylindrical buoy as described in Palm et al. (2016) and Paredes et al. (2016), shown in Fig. 2. The cylinder has a diameter $D = 0.515$ m, height $h = 0.4$ m, mass $M = 35.85$ kg and moment of inertia around the centre of gravity $I_{xx} = 0.9$ kg m². It is anchored to the bottom with three mooring cables, placed symmetrically 120° apart, with one cable attached on the leeward side directed along the propagation direction of the waves. Each mooring line is 1.95 m. long and anchored to the ground at a distance of 1.66 m. from the buoy. The mooring lines numerical properties are fully described in Palm et al. (2016). A wave probe is placed in the middle of the wave tank, 2.0 m away from the WEC, to measure surface elevation which is not only the incoming wave, but also radiated, diffracted and reflected waves.

The mooring system is modelled by means of the Moody library (Palm et al., 2017) and the numerical parameters are compiled from measurable quantities given in Paredes et al. (2016). The $k-\omega$ -SST model from Larsen and Fuhrman (2018) has been used for turbulence modelling as it provides a stable solution for the over production of turbulence levels beneath waves.

MULES is used to solve the VoF equation and the PIMPLE algorithm to solve the velocity-pressure coupling in the fundamental equations. In order to prove the robustness of the Overset mesh method with the Moody library, the resulting acceleration from the 6-DoF solver in OpenFOAM is not damped or reduced by any means.

3.3. Tests

Following Palm et al. (2016), five decay tests and two catalogue of regular waves are performed to demonstrate the capability of the numerical model. First, two decay tests without mooring (test *UT1* and test *UT2* from Table 2.) and three decay tests with moorings (test *MT1*, test *MT2* and test *MT3* from Table 2.) are simulated and analysed.

Table 4
Convergence based on discrimination ratio R_D .

Type	Convergence	Divergence
Monotonic	$0 < R_D < 1$	$R_D < 0$ and $ R_D < 1$
Oscillatory	$R_D > 1$	$R_D < 0$ and $ R_D > 1$

Next, two sets of experiments of regular waves will be performed to test the accuracy of the numerical software (test *MRW1* and test *MRW2* from Table 2.).

3.3.1. Free decay

The geometry of the NWT is based on the experimental wave basin described in Palm et al. (2016), with a slight modification made to increase the width of the NWT in order to avoid the reflections from the side walls. The NWT is depicted in Fig. 2 and is 8 m long, 8 m wide, 2 m high. Initial water level (IWL) is set to 0.9 m.

The four walls are defined as absorption boundaries (shallow water absorption condition). The bottom is defined as a non-slip boundary and the top as an open boundary.

3.3.2. Regular waves

The dimensions of the NWT are reduced in this case in order to minimise the computational costs. The basin is now 6 m long, 5 m wide, 2 m high (IWL = 0.9 m). As it can be observed the numerical domain is defined the same as the one used in Palm et al. (2016), without including the relaxation zones.

Wave generation (Stokes 5th order waves) and active absorption (shallow water active absorption boundary) are set at the inlet, and absorption (shallow water active absorption boundary) has been set at the outlet of the domain. Walls are defined as slip boundaries, the bottom as a non-slip boundary and the top as an open boundary.

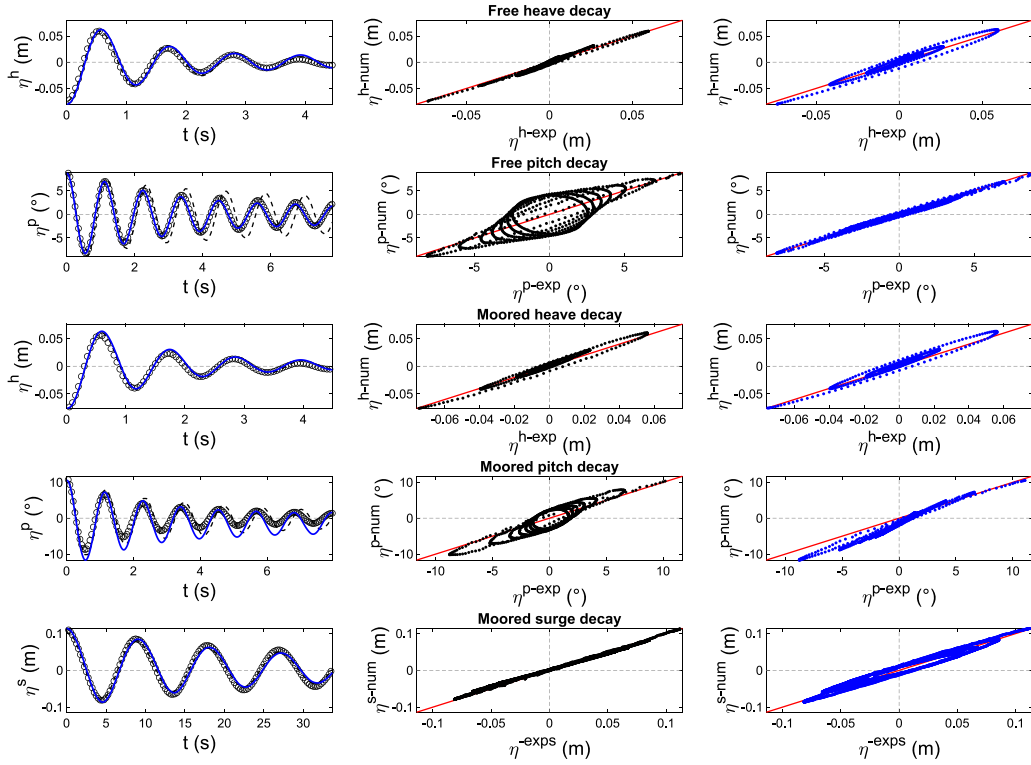


Fig. 3. Validation of decay tests, present work (blue line), numerical (dashed black line) and experimental (black dots) by Palm et al. (2016). The red line represents the bisector line. Left panels (numerical comparison between present work and by Palm et al., 2016), middle panels (comparison between numerical and experimental work by Palm et al., 2016) and right panels (comparison between present work and experiments by Palm et al., 2016). First line (free buoy when released from a given excitation in heave, $\delta = 0,075$ m), second line (free buoy when released from a given excitation in pitch, $\delta = 9.898^\circ$); third line (moored buoy when released from a given excitation in heave, $\delta = 0,076$ m), fourth line (moored buoy when released from a given excitation in pitch, $\delta = 11.353^\circ$) and fifth line (moored buoy when released from a given excitation in surge, $\delta = 0,114$ m).

Table 5

Relative discretisation uncertainty, U [%].

Parameter	M1	M2	M3	U [%]
1MHe	0.3017	0.0027	0.0017	0.25
2mHe	0.1875	0.0015	0.00066	0.7217

3.4. Grid analysis

A preliminary grid refinement study is carried out, following the approach described in Roache (1997), Stern et al. (2001) and Vukčević (2016). Three grids, $M1$ (coarse mesh), $M2$ (medium mesh) and $M3$ (fine mesh) (Table 3), are used in order to establish the total uncertainty arising from temporal and spatial discretisation errors. Mesh refinement can lead to instabilities within the overset framework in OpenFOAM for long displacements of the WEC. This is because the overset mesh method relies on interpolation between the overlapping regions of the meshes. To the author's knowledge there is not any rule whose fulfilment is compulsory when defining the cell size in the background mesh and in the overset mesh. For minimising any possible source of error when interpolation data between the background mesh and the overset mesh, resolution between the background and the overset mesh is maintained similarly in the three meshes. Following the work by Khan et al. (2024), the difference between experimental data and numerical data in the first maximum heave extreme (1MHe) and the first minimum heave extreme (2mHe) of the heave signal in a decay test, is used as the significant quantity for each grid size.

To analyse the convergence or divergence of the grid analysis, the discrimination ratio R_D is compute following (Vukčević, 2016):

$$R_D = \frac{(F_d - M_d)}{(M_d - C_d)} \quad (11)$$

where F_d is the solution of the finest mesh ($M3$), M_d is the solution of the medium mesh ($M2$) and C_d is the solution of the coarser mesh ($M1$). Table 4 summarises the four types of convergence.

The absolute grid uncertainty U_a , can be calculated for monotonic convergence:

$$U_a = F_s \frac{(F_d - M_d)}{(r^p - 1)}, \quad (12)$$

where F_s is the safety factor (1.5), an p is the order of accuracy:

$$p = \frac{\ln \frac{(F_d - M_d)}{(M_d - C_d)}}{\ln(r)}, \quad (13)$$

In the case of oscillatory convergence, the uncertainty is calculated following Stern et al. (2001):

$$U_a = F_s 0.5 |S_{max} - S_{min}|, \quad (14)$$

where S_{max} is the maxim solution and S_{min} is the minimum solution of the three meshes (fine, medium and coarse).

Following (Table 5), R_D proves monotone convergence for both the examined parameters ($R_D = 0.0033$ for 1MHe for and $R_D = 0.0045$ for 2mHe), with a resulting relative grid uncertainty of $U_a = 0.25\%$ for 1MHe and $U_a = 0.7217\%$ for 2mHe, which shows a satisfactory level of convergence. Cell resolution from the medium mesh $M2$ (Table 3) will be used in all the test cases in this work, as it combines accuracy and computational cost more efficiently than the other two discretisations ($M1$ and $M3$).

3.5. Results

3.5.1. Free decay test of an unmoored WEC

First, the hydrodynamic response of a free buoy is presented when released from a given excitation in heave (initial offset $\delta = 0.075$ m, test

Table 6

Quantitative comparison, Normalized Mean Squared Error (NMSE) between numerical and experimental (Palm et al., 2016) signals, and present work and experimental (Palm et al., 2016) signal.

Test	Parameter	Palm et al. (2016) (NMSE)	Present work (NMSE)
Decay	Free heave decay	0.0363	0.0396
Decay	Free pitch decay	0.4124	0.0202
Decay	Moored heave decay	0.0489	0.0573
Decay	Moored pitch decay	0.2874	0.2039
Decay	Moored surge decay	0.0158	0.0395
Regular (H = 0.04 m, T = 1.0 s)	Water free surface	0.0302	0.5696
Regular (H = 0.04 m, T = 1.0 s)	Moored surge	0.4715	0.5962
Regular (H = 0.04 m, T = 1.0 s)	Moored heave	0.3289	0.0263
Regular (H = 0.04 m, T = 1.0 s)	Moored pitch	0.3902	0.0951
Regular (H = 0.04 m, T = 1.2 s)	Water free surface	0.0422	0.0732
Regular (H = 0.04 m, T = 1.2 s)	Moored surge	0.9186	1.3539
Regular (H = 0.04 m, T = 1.2 s)	Moored heave	0.2051	0.123
Regular (H = 0.04 m, T = 1.2 s)	Moored pitch	0.2737	0.1666
Regular (H = 0.04 m, T = 1.4 s)	Water free surface	0.0048	0.0429
Regular (H = 0.04 m, T = 1.4 s)	Moored surge	0.5038	0.8042
Regular (H = 0.04 m, T = 1.4 s)	Moored heave	0.0075	0.0198
Regular (H = 0.04 m, T = 1.4 s)	Moored pitch	0.1166	0.0370
Regular (H = 0.08 m, T = 1.0 s)	Water free surface	0.0095	0.1908
Regular (H = 0.08 m, T = 1.0 s)	Moored surge	2.2400	1.8846
Regular (H = 0.08 m, T = 1.0 s)	Moored heave	0.0445	0.1080
Regular (H = 0.08 m, T = 1.0 s)	Moored pitch	0.2755	0.3234
Regular (H = 0.08 m, T = 1.2 s)	Water free surface	0.0833	0.2213
Regular (H = 0.08 m, T = 1.2 s)	Moored surge	0.2204	0.3693
Regular (H = 0.08 m, T = 1.2 s)	Moored heave	0.0991	0.0972
Regular (H = 0.08 m, T = 1.2 s)	Moored pitch	0.0783	0.0684
Regular (H = 0.08 m, T = 1.4 s)	Water free surface	0.0051	0.0947
Regular (H = 0.08 m, T = 1.4 s)	Moored surge	0.4201	0.3027
Regular (H = 0.08 m, T = 1.4 s)	Moored heave	0.0116	0.0831
Regular (H = 0.08 m, T = 1.4 s)	Moored pitch	0.0237	0.0392

UT1 from Table 2) and pitch (initial offset $\delta = 9.898^\circ$, test *UT2* from Table 2). Time series of comparison between the present work (Overset mesh method) and the numerical (deforming grid) and experimental work carried out by Palm et al. (2016) are shown in Fig. 3 (left panels). Present work (blue line) and the numerical work (black line) and the experimental (red line) by Palm et al. (2016) will be adopted in the upcoming validations. As it is a free buoy, no mooring restraints are attached.

The responses from both CFD techniques (deforming mesh and Overset mesh technique) are in good agreement. The damping of the oscillation obtained from the Overset mesh technique is similar to the results from the mesh morphing method and the numerical experiments.

In order to quantify the agreement between the previous results of Palm et al. (2016) and the present work, the parameter NMSE (Normalized Mean Squared Error) between numerical and experimental signals has been calculated (Table 6). The error from the free heave decay test are of the same order of magnitude, while for the free pitch decay test, the present work shows a higher degree of agreement between the two sets of data (NMSE = 0.0202) than Palm et al. (2016) (NMSE = 0.4124).

All the simulations in this work are performed using IHCantabria main supercomputing resource, named Neptune, which consists of a combination of servers that includes 1296 compute cores and over 5TB of RAM. In addition, it has a high-capacity, low-latency Infiniband FDR10 network, which allows these resources to be efficiently interconnected, functioning as a single computing unit. The final numerical mesh (2.2M cells) was partitioned to be run in parallel in 8 processors, taking 4 days to numerically simulate 3 s.

3.5.2. Free decay test of a moored WEC

Next, the hydrodynamic response of a moored buoy is presented when it is released from a given excitation in surge (initial offset $\delta = 0.114$ m, test *MT1* from Table 2), heave (initial offset $\delta = 0.076$ m, test *MT2* from Table 2) and pitch (initial offset $\delta = 11.353^\circ$, test *MT3* from

Table 2). Time series of comparison between the present work (Overset mesh method) and the numerical (deforming grid) and experimental work carried out by Palm et al. (2016) are displayed in Fig. 3 (right panels). It is observable that there is a good agreement between the present work and the experimental and previous numerical results. Moreover, the period of oscillation for both numerical techniques (deforming mesh and Overset mesh technique) are the same for the three cases.

The surge and heave response are equally damped than the experimental results for both numerical approaches (Fig. 3, right-top panel and right-medium panel). It can be seen a difference in the amplitude of the oscillations for the pitch decay case (Fig. 3, right-bottom panel) between both numerical approaches and the experiments. The results from the present work are in phase with the experimental data.

Overall, a good agreement has been achieved with both numerical approaches, resulting in quantified errors of the same order of magnitude (Table 6).

The final numerical mesh (4.3M cells) was partitioned to be run in parallel in 16 processors, taking 4 days to numerically simulate 5 s.

3.5.3. Regular waves interaction with a moored WEC

In this section, numerical simulations of the moored buoy interacting with regular waves are compared. Two sets of experiments are carried out with different wave heights ($H = 0.04$ m and $H = 0.08$ m), each of them with three different periods ($T = 1.0$ s, $T = 1.2$ s and $T = 1.4$ s), tests *MRW1* and *MRW2* from Table 2. The waves are generated accordingly to the fifth-order Stokes theory.

The same numerical solver and numerical parameters are used from the previous sections. Medium mesh (*M2*) discretisation was used. Therefore, the background domain and the moving domain are characterised by a cell resolution of 0.024 m along the x and y directions, and 0.008 m along the z direction. The computational domain is discretised into a structured grid and it contains 13.4M cells. Thus, the buoy was surrounded by 3 m of free computational domain on both sides of its initial position. Appendix A presents the surface elevation and the

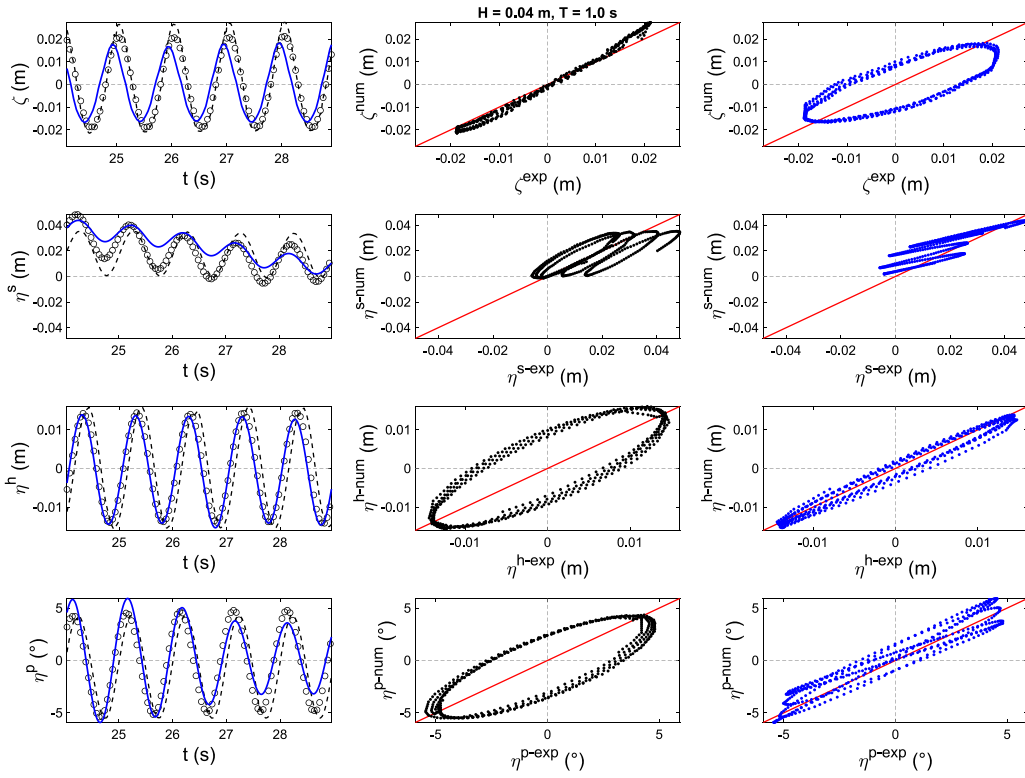


Fig. 4. Regular waves with target wave height $H = 0.04$ m and $T = 1.0$ s. Present work (blue line), numerical (dashed black line) and experimental (black dots) by Palm et al. (2016). The red line represents the bisector line. Left panels (numerical comparison between present work and by Palm et al., 2016), middle panels (comparison between numerical and experimental work by Palm et al., 2016) and right panels (comparison between present work and experiments by Palm et al., 2016). First line (wave elevation), second line (surge); third line (heave), and fourth line (pitch).

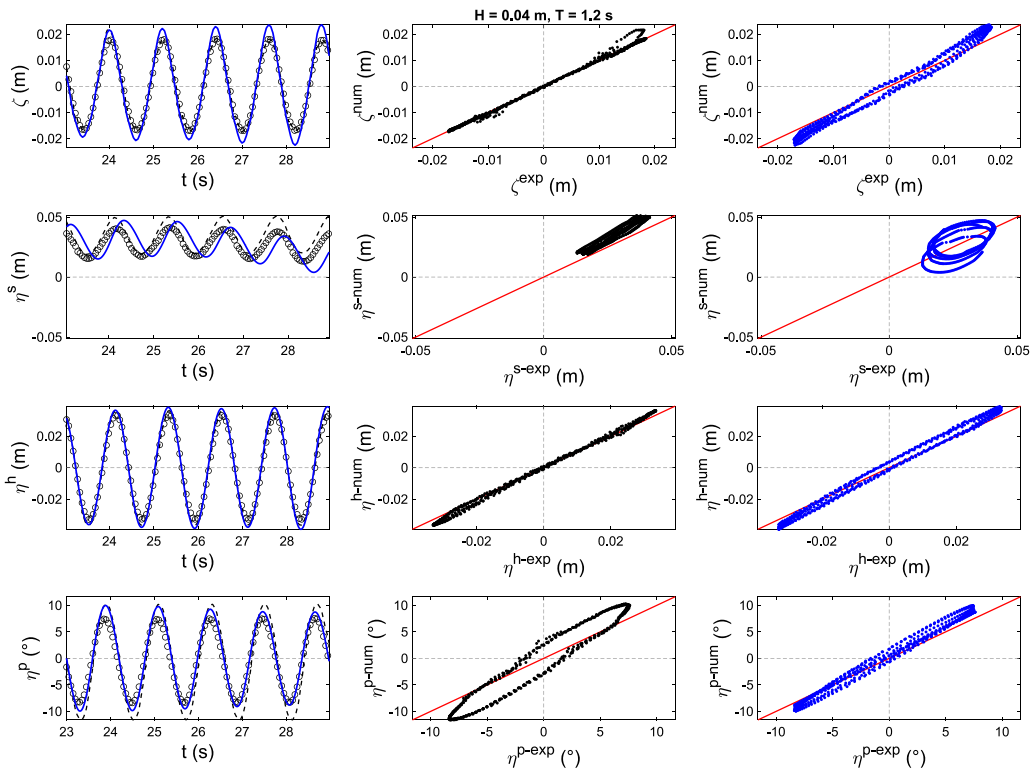


Fig. 5. Regular waves with target wave height $H = 0.04$ m and $T = 1.2$ s. Present work (blue line), numerical (dashed black line) and experimental (black dots) by Palm et al. (2016). The red line represents the bisector line. Left panels (numerical comparison between present work and by Palm et al., 2016), middle panels (comparison between numerical and experimental work by Palm et al., 2016) and right panels (comparison between present work and experiments by Palm et al., 2016). First line (wave elevation), second line (surge); third line (heave), and fourth line (pitch).

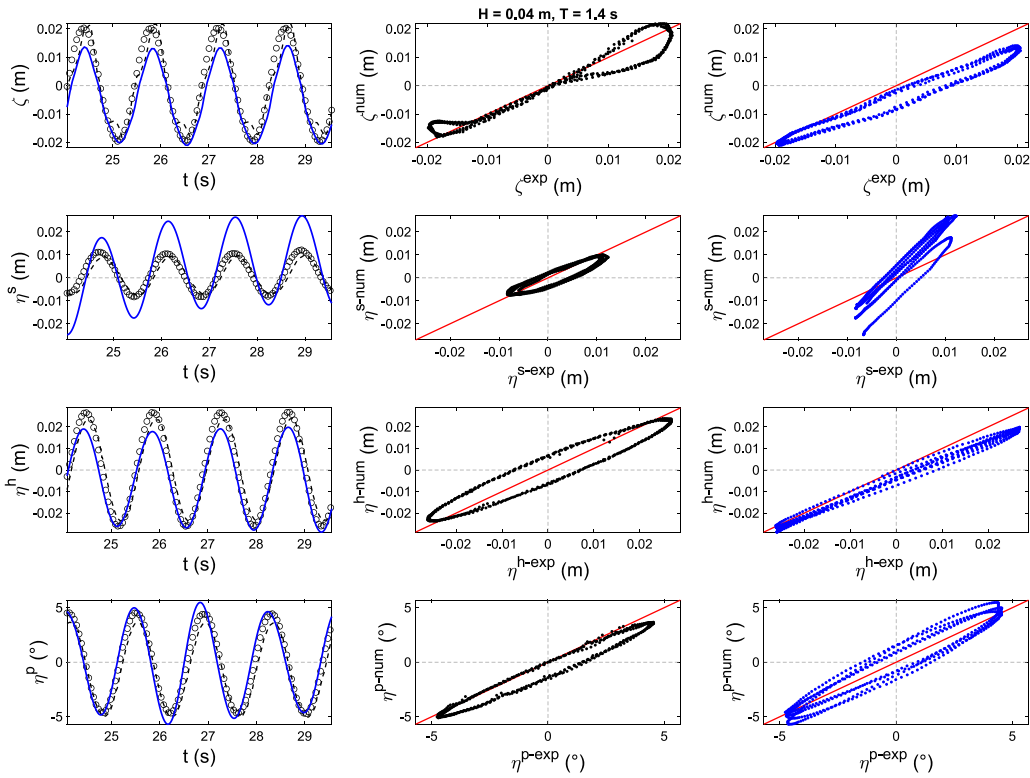


Fig. 6. Regular waves with target wave height $H = 0.04 \text{ m}$ and $T = 1.4 \text{ s}$. Present work (blue line), numerical (dashed black line) and experimental (black dots) by Palm et al. (2016). The red line represents the bisector line. Left panels (numerical comparison between present work and by Palm et al., 2016), middle panels (comparison between numerical and experimental work by Palm et al., 2016) and right panels (comparison between present work and experiments by Palm et al. (2016)). First line (wave elevation), second line (surge); third line (heave), and fourth line (pitch).

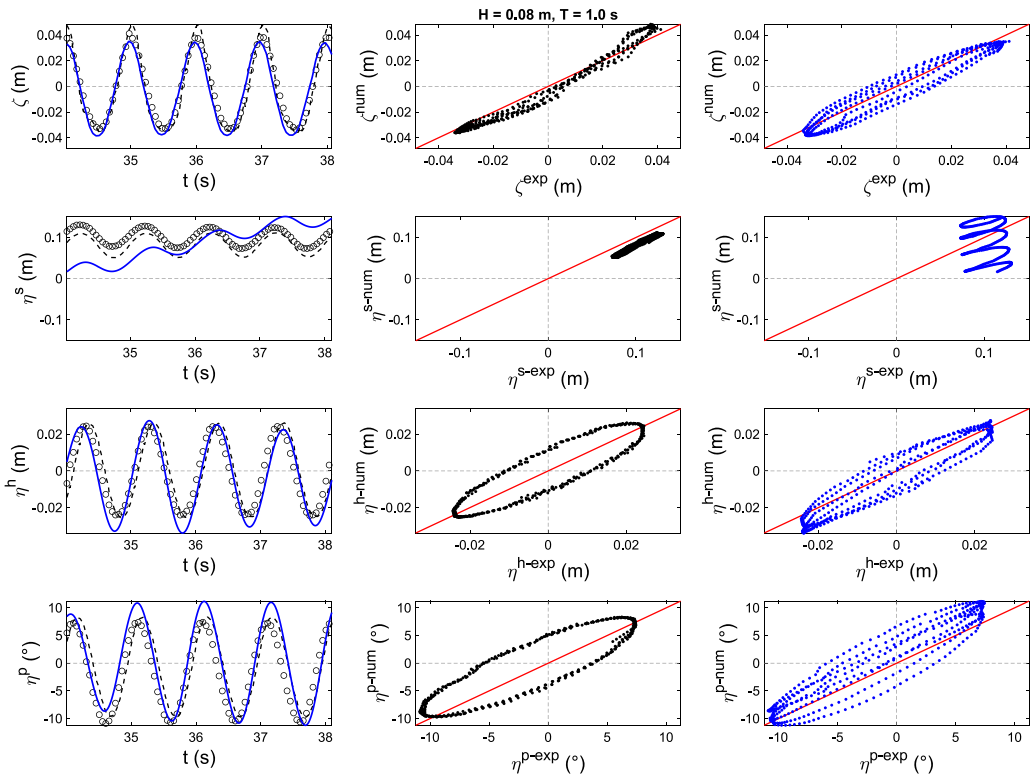


Fig. 7. Regular waves with target wave height $H = 0.08 \text{ m}$ and $T = 1.0 \text{ s}$. Present work (blue line), numerical (dashed black line) and experimental (black dots) by Palm et al. (2016). The red line represents the bisector line. Left panels (numerical comparison between present work and by Palm et al. (2016)), middle panels (comparison between numerical and experimental work by Palm et al. (2016)) and right panels (comparison between present work and experiments by Palm et al. (2016)). First line (wave elevation), second line (surge); third line (heave), and fourth line (pitch).

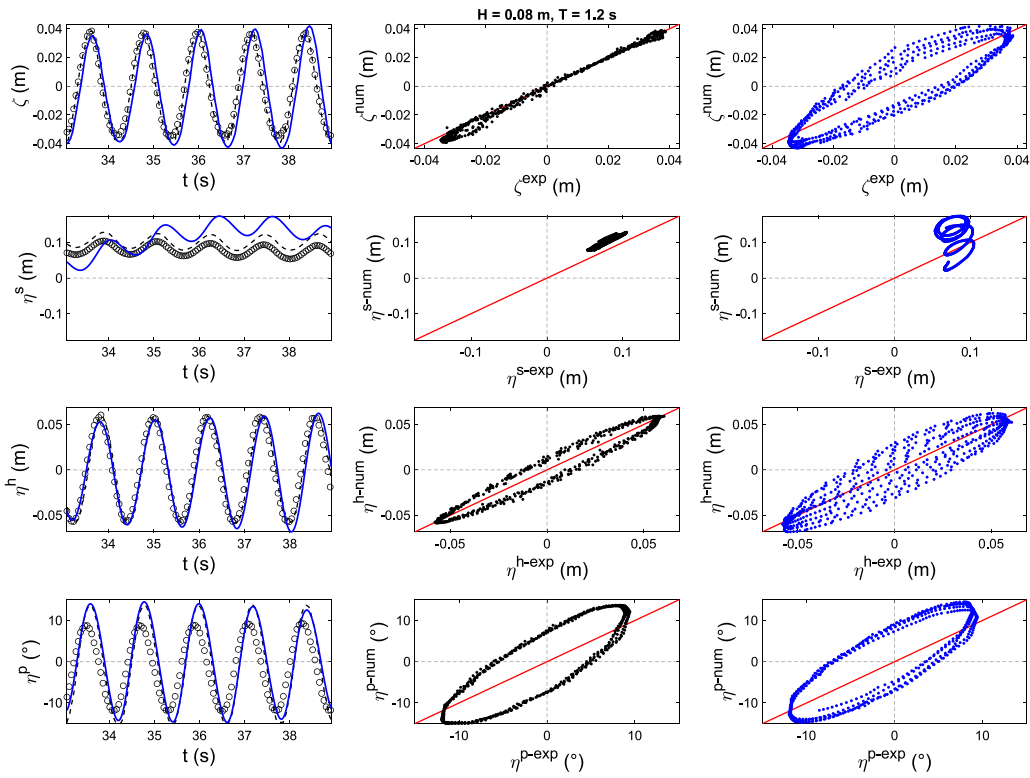


Fig. 8. Regular waves with target wave height $H = 0.08 \text{ m}$ and $T = 1.2 \text{ s}$. Present work (blue line), numerical (dashed black line) and experimental (black dots) by Palm et al. (2016). The red line represents the bisector line. Left panels (numerical comparison between present work and by Palm et al., 2016), middle panels (comparison between numerical and experimental work by Palm et al., 2016) and right panels (comparison between present work and experiments by Palm et al., 2016). First line (wave elevation), second line (surge); third line (heave), and fourth line (pitch).

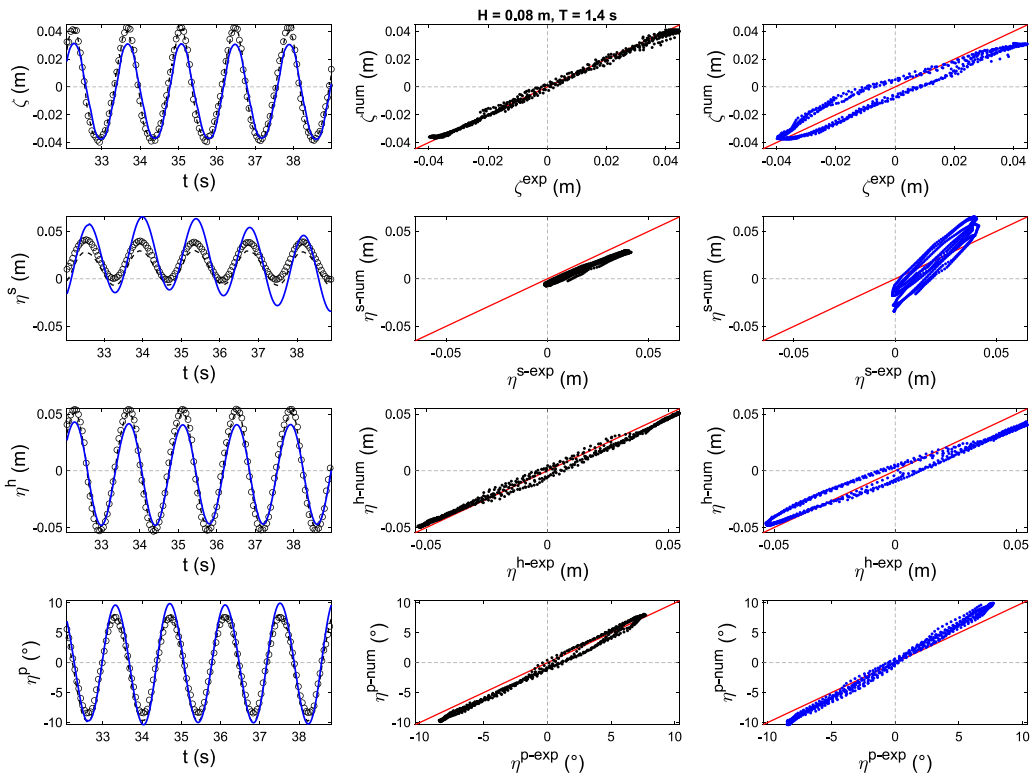


Fig. 9. Regular waves with target wave height $H = 0.08 \text{ m}$ and $T = 1.4 \text{ s}$. Present work (blue line), numerical (dashed black line) and experimental (black dots) by Palm et al. (2016). The red line represents the bisector line. Left panels (numerical comparison between present work and by Palm et al., 2016), middle panels (comparison between numerical and experimental work by Palm et al., 2016) and right panels (comparison between present work and experiments by Palm et al., 2016). First line (wave elevation), second line (surge); third line (heave), and fourth line (pitch).

Table 7

Quantitative comparison, Normalized Mean Squared Error (NMSE) between numerical and experimental (Palm et al., 2016) tensions, and present work and experimental (Palm et al., 2016) signal.

Test	Parameter	Palm et al. (2016) (NMSE)	Present work (NMSE)
Regular (H = 0.04 m, T = 1.2 s)	Tension L1	0.1917	0.3324
Regular (H = 0.04 m, T = 1.2 s)	Tension L2	0.6643	0.5307
Regular (H = 0.08 m, T = 1.2 s)	Tension L1	0.0658	0.4890
Regular (H = 0.08 m, T = 1.2 s)	Tension L1	0.4659	0.8672

velocity magnitude on the free surface and the displacement of the WEC when interacting with regular waves. The final numerical mesh (13.4M cells) was partitioned to be run in parallel in 64 processors, taking 20 days to numerically simulate 30 s.

Time series of comparison between the present work and the numerical and experimental work carried out by Palm et al. (2016) for 3 wave periods are analysed. Figs. 4, 5, 6, for wave target H = 0.04 m, and 7, 8, 9, for wave target H = 0.08 m shows the wave elevation of the incoming waves, and the response in surge, heave and pitch of the moored floating buoy for the two sets of regular waves simulated. Present work (blue line) and the numerical work (dashed black line) and the experimental (black dots) by Palm et al. (2016). The quantitative comparison is collated in Table 6.

In analysing the results of our simulations, we observed that the accuracy of wave propagation in our numerical model is lower compared to the results presented by Palm et al. (2016). Specifically, the NMSE values for the free surface elevation are higher in our simulations. This discrepancy primarily arises from differences in mesh resolution and refinement strategies employed in the two studies. In our simulations, we conducted a mesh convergence study based on the free decay experiment and then applied this mesh resolution uniformly across all simulations, including the wave interaction cases, to maintain consistency and manage computational resources effectively. Our mesh resolution is coarser than that used by Palm et al. (2016), who implemented significant mesh refinement near the free surface to enhance the accuracy of wave propagation. Our primary focus was on the dynamic response of the floating body, the effects of the PTO damping, and the integration of the mooring model within the overset framework. We acknowledge that a finer mesh near the free surface would improve the accuracy of wave propagation in our simulations, however the mesh resolution we employed was sufficient to capture the essential physics of the floating body's motion and the fluid-structure interactions pertinent to our study.

Overall good agreement with the experimentally measured motions is observed, with the exception is the surge motion. These anomalous surge results were also noticed by Palm et al. (2016), stemming from an oscillation generated by a sudden displacement of the wave paddle because of the choice of a small ramping time in order to reduce the computational. Firstly, the amplitude of surge oscillation at the wave frequency is underpredicted for the $T = 1.0$ s case, approximately equivalent for the $T = 1.2$ s case and overpredicted for the $T = 1.4$ s case. Secondly, there is a low frequency oscillation component, corresponding to the surge natural frequency, superposed with the wave frequency oscillation, that is not evident in Palm et al. (2016)'s results. The reason for the first difference is unknown, considering the other DoFs agree well for these cases and so too does the surge free decay results. The second difference is possibly due to our simulations using a less gradual ramp-up time for the input wave than was used in Palm et al. (2016) (the full time series is not shown), which excited a transient oscillation in the surge dynamics.

Appendix B presents the time histories of tension force in the seaward cable and leeward for $T = 1.2$ s ($H = 0.04$ m and $H = 0.08$ m). Both experimental values and numerical simulations are presented. The quantitative comparison is collated in Table 7

Table 8

Influence of the different characterisation of the PTO damping (varying the porosity) in the maximum displacements in heave (m) and period of oscillations (s). Cases *MTP*.

Porosity configuration	Porosity n (-)	Maximum displacement z (m)	Period T (s)
Porosity1 (P1)	0.05	0.1196	1.0460
Porosity2 (P2)	0.25	0.1192	1.0354
Porosity3 (P3)	0.50	0.1187	1.0385
Porosity4 (P4)	0.75	0.1185	1.0358
Porosity5 (P5)	1.00	0.1172	1.0391

Table 9

Final displacement of the WEC.

$U_c \setminus$ Porosity	0.25 (-)	0.50 (-)	0.75 (-)	1.00 (-)
0.25 (m/s)	0.120	0.119	0.117	0.123
0.50 (m/s)	0.284	0.283	0.282	0.279
0.75 (m/s)	0.370	0.373	0.374	0.374
1.00 (m/s)	0.420	0.438	0.439	0.441

4. Simulation of a floating OWC

Once that the overset framework in OpenFOAM has been proved to accurately reproduce the interaction of a moored WEC under free (Section 3.5.1) and moored (Section 3.5.2) decay tests and with regular waves (Section 3.5.3), the primary objective of the present work is to demonstrate that the PTO damping can be numerically modelled as a porous media in order to prove that it has very little influence in the main displacements of a WEC.

4.1. Case study

Following the work by Palm et al. (2016), a modified WEC with a numerical PTO is modelised. As stated by Iturrioz et al. (2015), the PTO can be conceptualised using a top slot which is able to simulate different resistances to the air circulating through it. Real PTOs commonly consist of a self-rectifying air turbine that imposes a resistance to the air flow and behaves as a damping force during the chamber charge and discharge processes. This damping force depends on the turbine type and the force exerted by the alternator. By varying the porosity of the PTO, different scenarios can be reproduced: fully open PTO ($n = 1.0$, not damping, as if the PTO is not considered), almost fully closed PTO ($n = 0.05$, the PTO is substituted by a rigid wall), and intermediate states ($0.05 < n < 1.0$). The biggest challenge to is to reproduce accurately the phenomena of fluid interaction with the chamber as well as its repercussion in the pneumatic processes.

4.2. Numerical wave tank

The new WEC has been defined as a hollow cylinder of outer diameter $D_1 = 0.515$ m and inner diameter of $d_1 = 0.25$ m, height $h_1 = 0.4$ m, mass $M = 27.4$ kg and moment of inertia around the centre of gravity $I_{xx} = 0.9$ kg m². The PTO is defined as a truncated cylinder of $d_2 = 0.25$ m and width $w_2 = 0.08$ m, placed inside the WEC and filling it completely in the upper part (Fig. 10, right panel). The WEC is anchored to the bottom with three mooring cables, placed

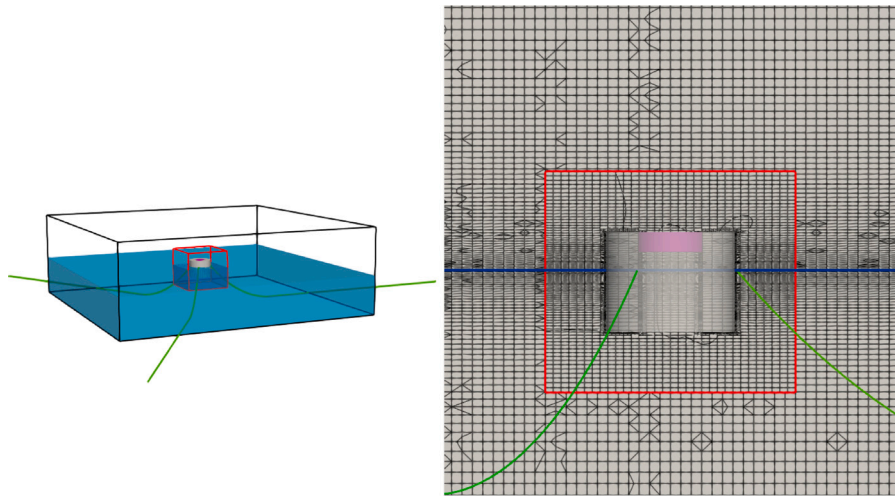


Fig. 10. Numerical domain (6 m long, 6 m wide and 2 m high) for heave decays varying the PTO damping defining different porosities, (Left panel), detail of cell size discretisation (right panel). The new WEC has been defined as a hollow cylinder of outer diameter $D_1 = 0.515$ m and inner diameter of $d_1 = 0.25$ m, height $h_1 = 0.4$ m. Initial water level is 0.9 m Moorings are in green, Overset domain is plotted in red, free surface is plotted in blue.

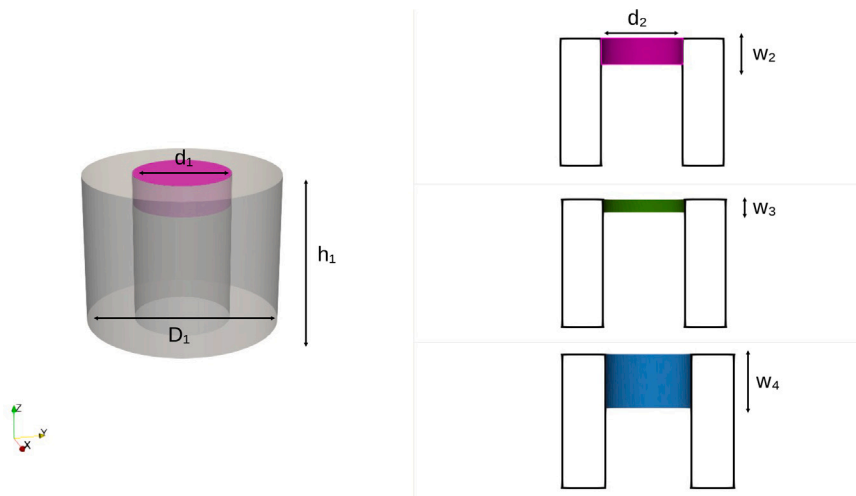


Fig. 11. Left panel, visualisation of the WEC defined as a hollow cylinder (opacity set to 50%) and the PTO as a truncated cylinder (purple). Right panels, side view (plane XZ) different PTO's characterisation varying the width (w_2 in purple, w_3 in green and w_4 in blue). WEC: Outer diameter D_1 [m], inner diameter d_1 , height h_1 . PTO: diameter d_2 [m], width w_2 , w_3 and w_4 [m].

symmetrically 120° apart, with one cable attached on the leeward side directed along the propagation direction of the waves (Fig. 10, left panel). As in the previous tests, the mooring system is modelled by means of the Moody library (Palm et al., 2017) and the numerical parameters are compiled from measurable quantities given in Paredes et al. (2016). An initial water depth of $h = 0.9$ m is defined. This results in a floating OWC geometry similar to that tested by Zhou et al. (2021b,c).

The dimensions of the NWT are reduced in this case regarding the validation cases, in order to minimise the computational costs. The numerical parameters are the same as the previous cases. $k-\omega$ -SST model from Larsen and Fuhrman (2018) is used for turbulence modelling, MULES algorithm to solve the VoF equation and the PIMPLE algorithm to solve the velocity-pressure coupling. The resulting acceleration from the 6-DoF solver in OpenFOAM is not damped or reduced by any means.

4.3. Tests

Three different tests are performed to demonstrate the capability of the numerical model:

1. **Free decay:** A series of heave free decay tests are performed with porous media zone used to implement the PTO damping, varying the zone of influence of the PTO (porous zone, tests *MTPW*) and the levels of damping (porosity value, tests *MTP*), from Table 2. These tests demonstrate the effect of the PTO damping on the floating body motion. As demonstrated in Tan et al. (2022) and Çelik and Altunkaynak (2020), changing the PTO damping in a heaving OWC or WEC will alter its natural frequency and maximum displacements.
2. **Input current:** A series of interaction of constant loading cases with a WEC are performed with porous media zone used to implement varying levels of PTO damping (tests *MTPC* from Table 2). Currents are used to highlight the overset mesh's ability to handle large displacements of the floating OWC within the computational domain and to demonstrate the ability of the PTO region to move coincidentally with the OWC, maintaining its correct position at the top of the OWC chamber. The input current also highlights the functionality and necessity of the mooring model.
3. **Regular waves:** A series of interaction of regular waves with a WEC, are performed with porous media zone used to implement

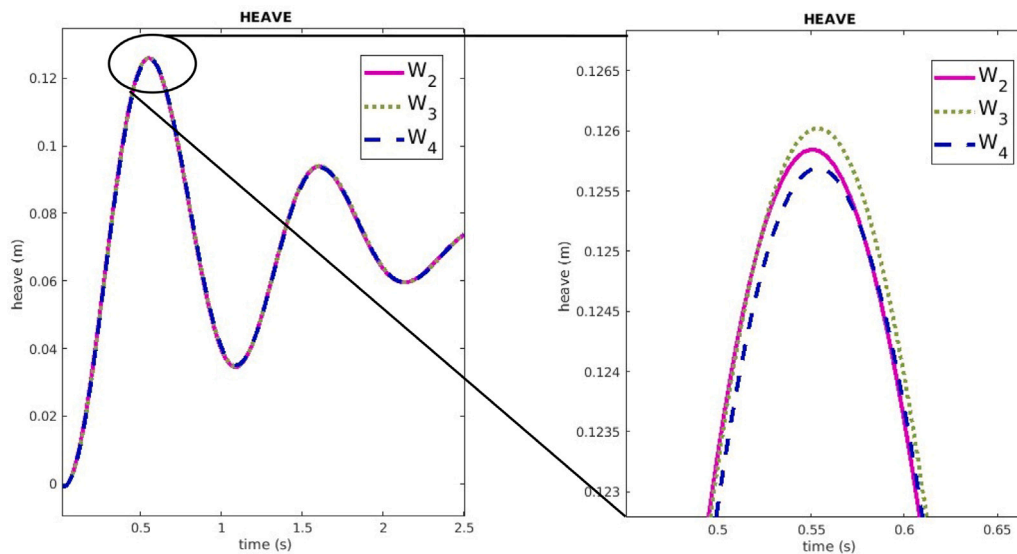


Fig. 12. Free decay test of the WEC with PTO over the time when released from a given excitation in heave, $\delta = 0,075$ m, with different PTO's characterisation varying the width (w_2 in purple, w_3 in green and w_4 in dashed blue).

varying levels of PTO damping (tests *MTPW* from Table 2). These scenarios replicate experimental cases in which WEC's are tested under realistic wave conditions of the zone in which they will be deployed, highlighting how numerical experiments are complementary to laboratory campaigns.

4.3.1. Free decay

The dimensions of the NWT are 6 m long, 6 m wide and 2 m high (IWL = 0.9 m). A refinement around the free surface has been added to accurately capture the motion of the fluid inside the hollow cylinder that represents the WEC, Fig. 10, right panel.

The four walls are defined as absorption boundaries (shallow water absorption condition). The bottom is defined as a non-slip boundary and the top as an open boundary.

Adding the PTO damping in a heaving OWC or WEC will alter its natural frequency and maximum displacements. However, as these changes will have very little influence in the main displacements of the moored WEC there is no need to carry out another grid analysis, provided that the new discretisations are either in the same order of magnitude or with smaller sizes, than the values obtained from the grid analysis in Section 3.4. The background domain and the moving domain are characterised by a cell resolution of 0.04 m along the x and y directions, and 0.02 m along the z direction. Cell size around the free-surface is refined to obtain a final discretisation of 0.006 m in the vertical direction. The computational domain is discretised into a structured grid and it contains 2.3M cells.

4.3.2. Input current

The dimensions of the NWT are 6 m long, 4 m wide and 2 m high (IWL = 0.9 m).

Flow generation (constant currents, $U_c = [0.25, 0.50, 0.75]$ in the main displacements of the moored WEC, 1.00] m/s) and active absorption (shallow water absorption boundary) are set at the inlet, and absorption (shallow water absorption boundary) has been set at the outlet of the domain. Walls are defined as slip boundaries, the bottom as a non-slip boundary and the top as an open boundary.

The background domain and the moving domain are characterised by a cell resolution of 0.0375 m along the x and y directions, and 0.0187 m along the z direction. The computational domain is discretised into a structured grid and it contains 1.8M cells.

4.3.3. Regular waves

The dimensions of the NWT are 6 m long, 4 m wide and 2 m high (IWL = 0.9 m).

Wave generation (5th order Stokes waves, $H = 0.2$ m, $T = 3.0$ s) and active absorption (shallow water absorption boundary) are set at the inlet, and absorption (shallow water absorption boundary) has been set at the outlet of the domain. Walls are defined as slip boundaries, the bottom as a non-slip boundary and the top as an open boundary.

As for the previous case, Section 4.3.2, the background domain and the moving domain are characterised by a cell resolution of 0.0375 m along the x and y directions, and 0.0187 m along the z direction. The computational domain is discretised into a structured grid and it contains 1.8M cells.

4.4. Results

4.4.1. Free decay test of moored WEC with PTO

In this section, the hydrodynamic response of a moored WEC with a PTO defined as a porous medium is presented when it is released from a given excitation in heave (initial offset $\delta = 0.075$ m).

First, a series of simulations varying the zone of influence of the PTO are performed (tests *MTPW*, from Table 2). The advantages of using damping numerical regions, instead of using the real geometry are mostly connected to computational savings, as stated by Gadelho et al. (2022). In the case of using damping numerical regions, the user only needs to change a certain range of parameters, as an iterative process, until obtaining the desired results. However, these types of approaches cannot replicate the flow in the vicinity of the PTO. Three different PTOs are simulated (Fig. 11, right panels) by reducing and enlarging the width of a defined value $w_2 = 0.08$ m ($w_3 = 0.03$ m and $w_4 = 0.115$ m) to analyse the influence in the simulations of the porous area. All the other numerical parameters are kept constant.

Defining the case with a PTO width of w_2 as the representative, it can be seen from Fig. 12, that increasing (case w_4) or decreasing (case w_3) the width of the porous area has very little influence in the period of the oscillations (no difference in the period of the first three oscillations). Heave responses are less damped for smaller widths of the porous area that defines the PTO (differences of 0.15% for both w_3 and w_4 , with respect to case w_2). This is caused because the influence of the PTO is less relevant for a case with a very small width (air flow is very little affected while passing through this damping area) than a case

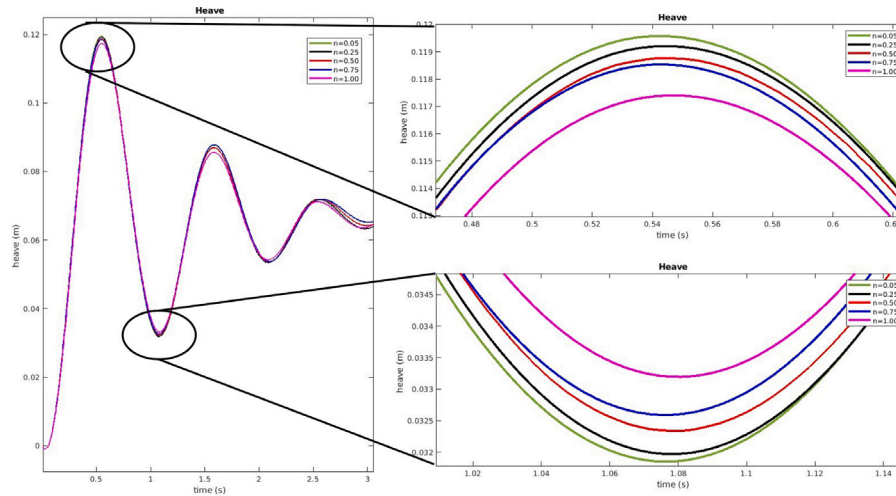


Fig. 13. Heave response over time for different PTO modelisations (varying porosity as in Table 8).

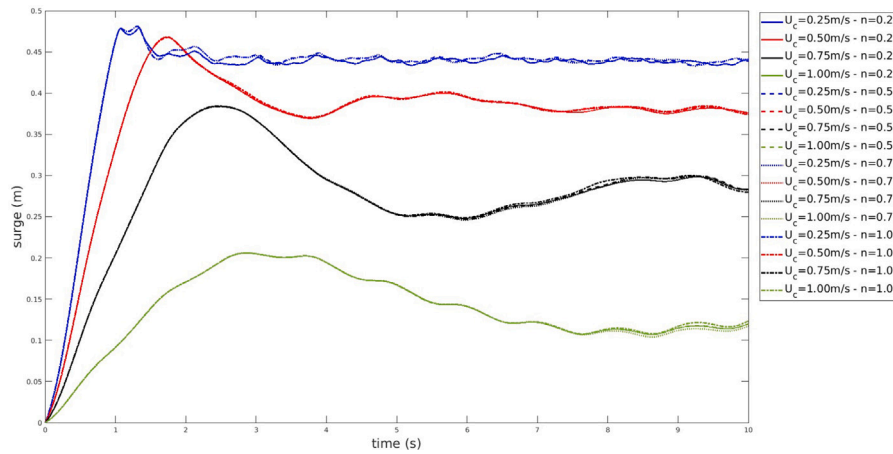


Fig. 14. Displacement of the WEC (surge) over the time under constant currents : $U_c = [0.25$ (green), 0.50 (black), 0.75 (red), 1.00 (blue)] m/s - $P = [0.25$ (continuous line), 0.50 (dashed line), 0.75 (dotted line), 1.00 (dashed-dotted line)].

with bigger width (once air has entered the porous area, its damped for longer time until it reaches the other boundary of the porous area).

The final numerical mesh (2.2M cells) was partitioned to be run in parallel in 8 processors, taking 5 days to numerically simulate 5 s.

Secondly, a catalog of simulations (tests *MTP*, from Table 2) varying the porosity are defined to assess the influence of a PTO in hydrodynamic response of a WEC (Table 8). Changing the porosity produces different PTO dampings. Choosing the same numerical configuration of the previous case and just changing the porosity n (all the other parameters that define the porous medium are kept constant, i.e., $a = 200$, $b = 10$, $c = 0.34$, $D_{50} = 0.0159$, and $KC = 1.0$), can lead to cases where the air flow is very influenced when passing through the PTO ($n = 0.05$) and cases where the air flow is not affected by the PTO ($n = 1$).

Fig. 13 shows that heave responses are less damped for smaller porosities because when the air cannot flow through the PTO is reflected and pushes the WEC upwards. On the other hand, heave responses are more damped for bigger porosities because the air can flow through the PTO and almost not interact with any part of the floating device. The maximum heave displacement is reported in Table 8 and it can be observed that the biggest displacement is for the smallest porosity ($n = 0.05$), $\delta_h = 0.1195$ m, and the minimum for the biggest porosity ($n = 1.0$), $\delta_h = 0.1174$ m as expected.

In addition, it can be observed a change in the period of oscillation, caused again by the interaction of the air when passing through the

PTO, as reported by Tan et al. (2022) and Çelik and Altunkaynak (2020). The period of oscillations is reported in Table 8, and differences are very small. It can be seen that including the damping caused by a PTO has a measurable influence in the numerical oscillations. The smaller porosity ($n = 0.05$) produces a displacement with the bigger period of oscillation ($T = 1.0460$ s). Appendix C presents a side view of the velocity contour lines a top view of the surface elevation for a free decay test of a moored WEC with PTO ($n = 0.5$).

The final numerical mesh (2.2M cells) was partitioned to be run in parallel in 8 processors, taking 4 days to numerically simulate 3 s.

4.4.2. Input current test of moored WEC with PTO

In this section, numerical simulations of the moored WEC with a PTO interacting with currents are shown. Four sets of simulations are compared varying the porosity ($n = [0.25, 0.50, 0.75, 1.00]$) and each of them will be simulated with four different current velocities ($U_c = [0.25$ m/s, 0.50 m/s, 0.75 m/s, 1.00 m/s]) to create a catalog of 16 conditions.

From Fig. 14, it can be seen that the displacement of the WEC with PTO is dominated by the strong current velocities imposed, and that the PTO has very little influence in the results, although it can be seen at the end of the simulation slight differences appear due to the different PTO characterisation (porosity values). When increasing the current magnitude, the displacement of the WEC is as well amplified. The bigger current, the faster the WEC reaches a steady state. For

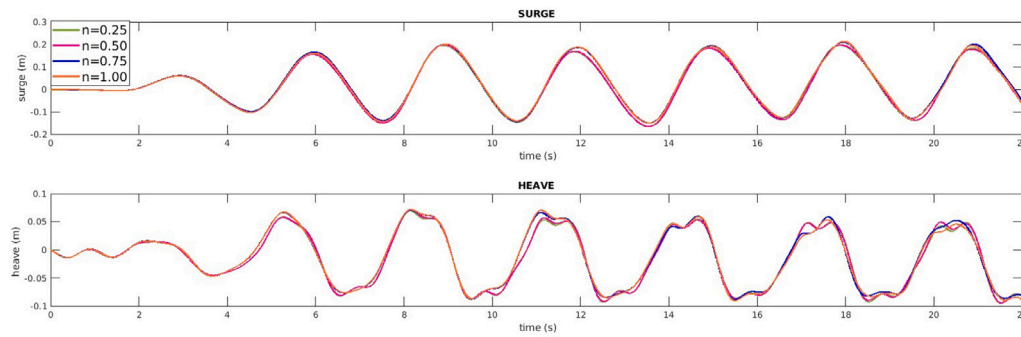


Fig. 15. Displacement of the WEC over the time (top panel surge and lower panel heave) under regular waves (5th order Stokes, $H = 0.2$ m, $T = 3.0$ s). Four different damping characterisations are tested: $n = [0.25$ (green), 0.50 (pink), 0.75 (blue), 1.00 (orange)].

Table 10
Maximum displacement of the WEC.

$U_c \backslash$ Porosity	0.25 (-)	0.50 (-)	0.75 (-)	1.00 (-)
0.25 (m/s)	0.206	0.206	0.206	0.206
0.50 (m/s)	0.384	0.384	0.384	0.384
0.75 (m/s)	0.468	0.468	0.468	0.467
1.00 (m/s)	0.480	0.481	0.481	0.479

the case with smaller currents, the difference between the maximum displacement and the steady case is bigger.

Final displacement of the WEC for the 16 cases that composes the catalog (four different current velocities, and for each, four different porosities to model the PTO) are reported in Table 9. There is not a clear tendency of the final displacement when varying the porosity for modelling the damping of a PTO. The mean final displacement for $U_c = 0.25$ m/s, is 0.120 m, for $U_c = 0.50$ m/s is 0.282 m, for $U_c = 0.75$ m/s, is 0.373 m, and for $U_c = 1.0$ m/s is 0.434 m. The differences for the four modelisations of the PTO for each current are very small and are influenced by the modelisation of the free-surface inside the WEC. There is strong gradient of the velocities in the vicinity of the WEC, specially behind the structure when hydraulic jumps are created, which will affect the correct interface capturing. Fig. 14 shows these periodic instabilities in the displacement of the WEC after the maximum displacement. Maximum displacement of the WEC is reported in Table 10. For each current magnitude, the maximum displacement is almost identical for the different modelisation of the PTO when varying the porosity. The mean maximum displacement for $U_c = 0.25$ m/s, is 0.206 m, for $U_c = 0.50$ m/s is 0.384 m, for $U_c = 0.75$ m/s, is 0.484 m, and for $U_c = 1.0$ m/s is 0.480 m. As it is a process which is dominated by the strong currents, bigger currents impose bigger final and maximum displacements. Again, it can be stated that the displacement is dominated by the currents, and that the PTO does not have a strong influence.

It can be seen that when increasing the current magnitude, the displacement of the WEC is as well amplified. For very big values, a hydraulic jump is created behind the structure, inducing nonlinear interactions with the floating body. Again, it can be seen that side walls do not have a significant influence on the flux around the body. Appendix D presents the final displacement of a moored WEC with PTO and the velocity magnitude on a plane, when interacting with constant loading's.

The final numerical mesh (1.8M cells) was partitioned to be run in parallel in 8 processors, taking 7 days to numerically simulate 10 s.

4.4.3. Regular waves interaction with a moored WEC with PTO

In this section, numerical simulations of the moored WEC with a PTO interacting with regular waves are shown. Four simulations are compared varying the porosity ($n = [0.25, 0.50, 0.75, 1.00]$), for 5th order Stokes regular waves ($H = 0.2$ m, $T = 3.0$ s).

From Fig. 15, it can be seen that the main displacements of the WEC (surge and heave) are influenced by the damping of the PTO. Regarding the surge evolution over time, the presence of the PTO alters the natural frequency. The mean oscillating period of surge for $n = 0.25$, is 2.998 s, for $n = 0.50$ is 2.994 s, for $n = 0.75$, is 2.991 s, and for $n = 1.0$ m/s is 2.972 s. Bigger damping caused by the PTO (therefore, the smallest value of porosity, $n = 0.5$), produces an oscillation very close to the generated waves (0.2% of difference). On the other hand, if there is no PTO damping (porosity $n = 1.0$), the oscillations in surge differ the most from the generated waves (0.9% of difference). Nevertheless, as expected in all cases, the differences are very small as the PTO damping has very little influence in the main displacements.

From Fig. 15 it can be seen that there is not a clear tendency of the maximum heave displacements of the WEC. This is due to the fact that the wave sloshing in combination with the air trapped inside the chamber produces a non-linear variation of the maximum heave displacement. However, two oscillations can be seen for each wave in all the four cases. Further analysis is required to understand this complex process, but as wave sloshing and air compressibility effects are not analysed in this work, this is beyond the scope of this work. Appendix E presents for the interaction of a WEC with PTO with regular waves, firstly a 3D view of surface elevation on the free surface and a 2D view of the velocity magnitude, and secondly a side view of the velocity contour lines for water and air.

The final numerical mesh (1.8M cells) was partitioned to be run in parallel in 8 processors, taking 15 days to numerically simulate 22 s.

5. Conclusions

This paper introduces a robust framework within the OpenFOAM to simulate the interaction of a wave energy converter with waves and currents. The PTO damping of a moored floating WEC is modelled by means of a new numerical approach. The advantage of this approach is the simple characterisation of the complex structure of a PTO, modelling the air-structure damping by means of frictional forces exerted by the porous media.

The first part of the present work focuses in the validation of the interaction of a moored floating wave energy converter in free and moored decay tests and under regular waves. The Overset framework is used for modelling the displacement of a WEC (Palm et al., 2016), Moody library (Palm et al., 2017) is used to compute the mooring restraints, and the IHFOAM (Higuera et al., 2013) suite to generate the boundary conditions. By analysing the decay tests and regular wave cases, it is remarkable a good agreement between the present work and the experimental data (Palm et al., 2016). Moreover, the comparison between two different numerical techniques for simulating moving bodies, deforming grid (Palm et al., 2016) and Overset mesh method (present work) show an overall good agreement between them and against the experimental data.

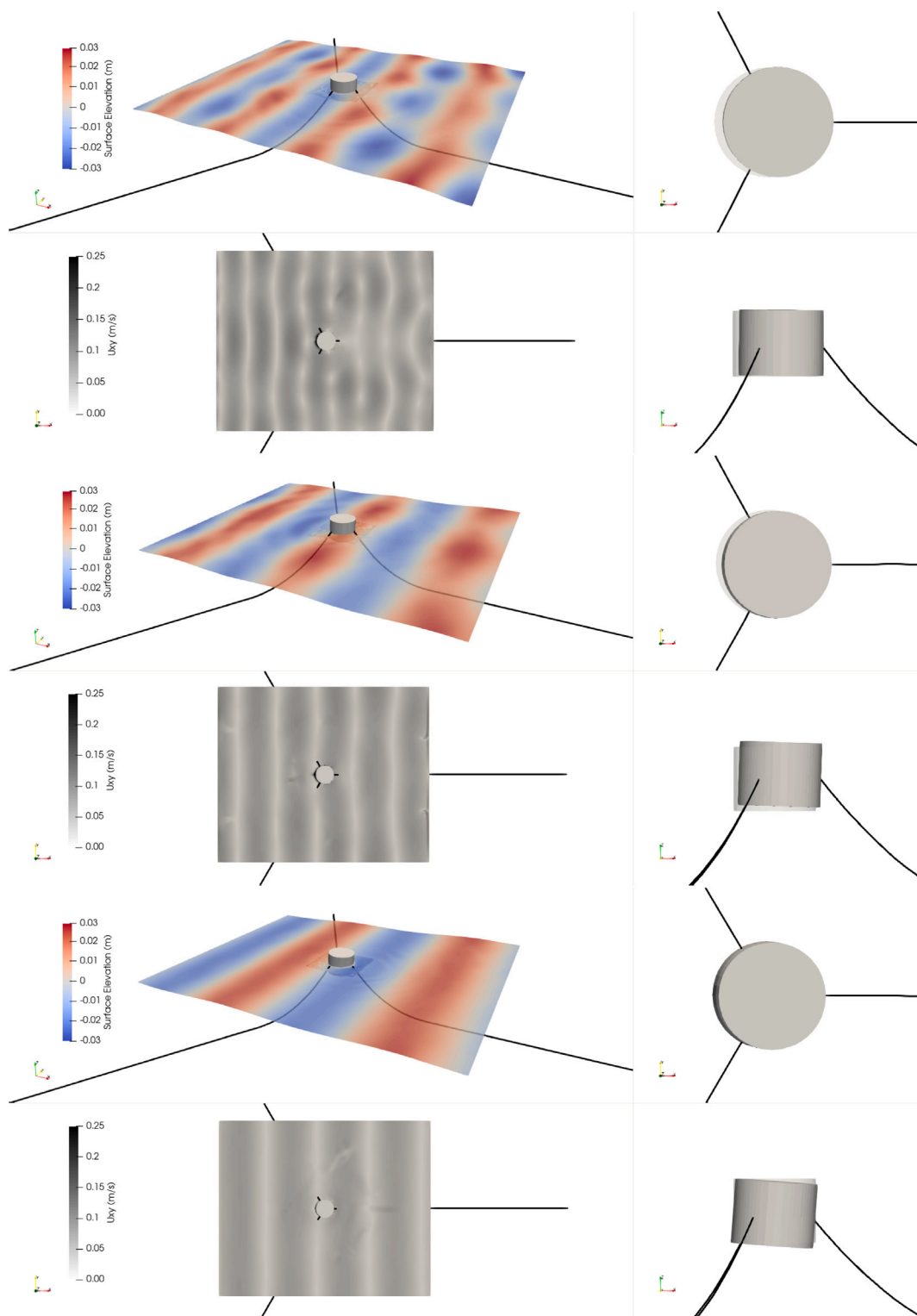


Fig. A.16. Top-left view (surface elevation plotted on the free surface, VoF = 0.5), bottom-left view (velocity magnitude, plane XY, $z = 0.8$ m), top-right (top view of the WEC, plane XY), bottom-right view (side view of the WEC, plane XZ). First case (for $H = 0.04$ m, $T = 1.0$ s), second case (for $H = 0.04$ m, $T = 1.2$ s) and third case (for $H = 0.04$ m, $T = 1.4$ s).

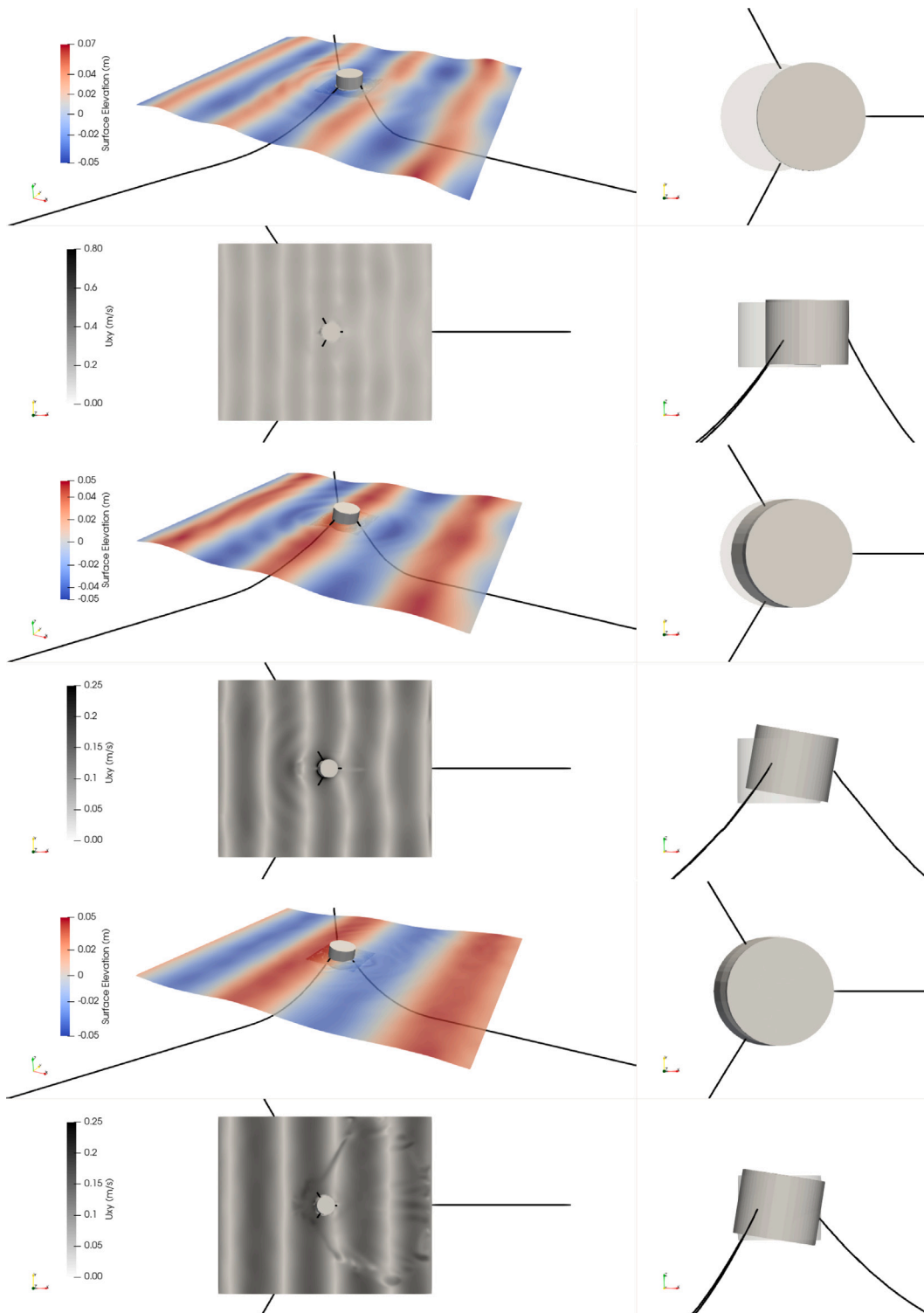


Fig. A.17. Top-left view (surface elevation plotted on the free surface, VoF = 0.5), bottom-left view (velocity magnitude, plane XY, $z = 0.8$ m), top-right (top view of the WEC, plane XY), bottom-right view (side view of the WEC, plane XZ). First case (for $H = 0.08$ m, $T = 1.0$ s), second case (for $H = 0.08$ m, $T = 1.2$ s) and third case (for $H = 0.08$ m, $T = 1.4$ s).

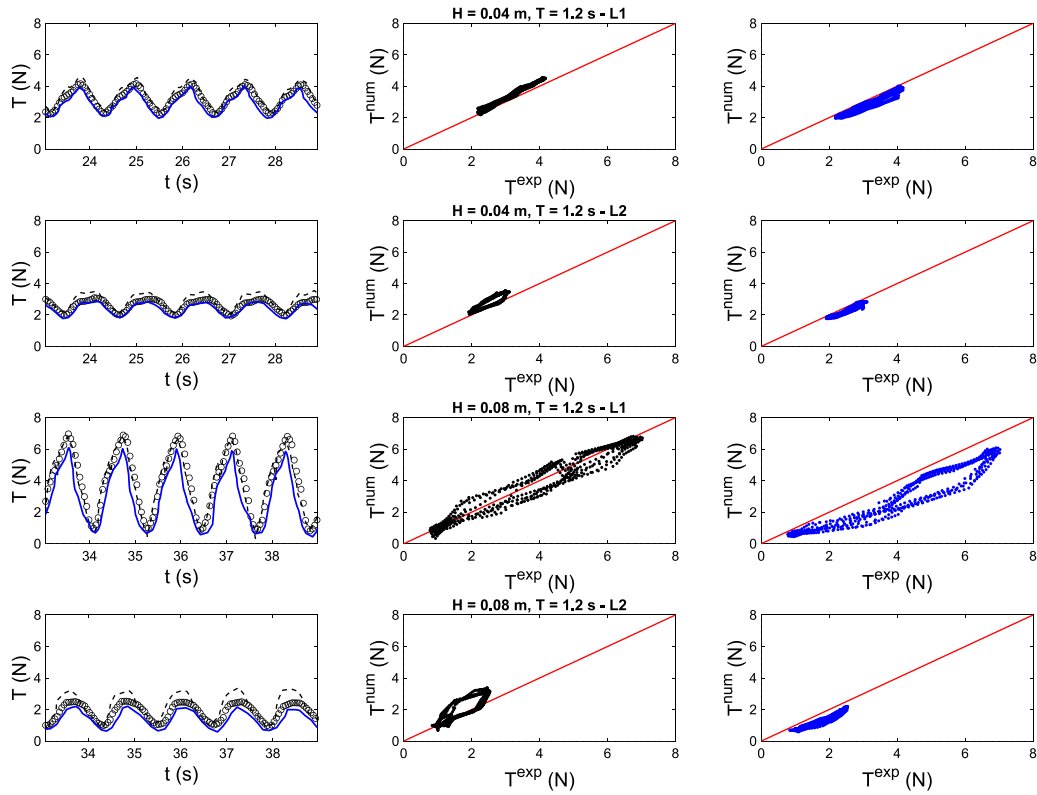


Fig. B.18. Time histories of tension forces for regular waves cases, with target wave height $H = 0.04$ m and $T = 1.2$ s and $H = 0.08$ m and $T = 1.2$ s Present work (blue line), numerical (dashed black line) and experimental (black dots) by Palm et al. (2016). The red line represents the bisector line. Left panels (numerical comparison between present work and by Palm et al. (2016)), middle panels (comparison between numerical and experimental work by Palm et al. (2016)) and right panels (comparison between present work and experiments by Palm et al. (2016)). First line (Leg 1, $H = 0.04$ m and $T = 1.2$ s), second line (Leg 2, $H = 0.04$ m and $T = 1.2$ s); third line(Leg 1, $H = 0.08$ m and $T = 1.2$ s), and fourth line (Leg 2, $H = 0.08$ m and $T = 1.2$ s).

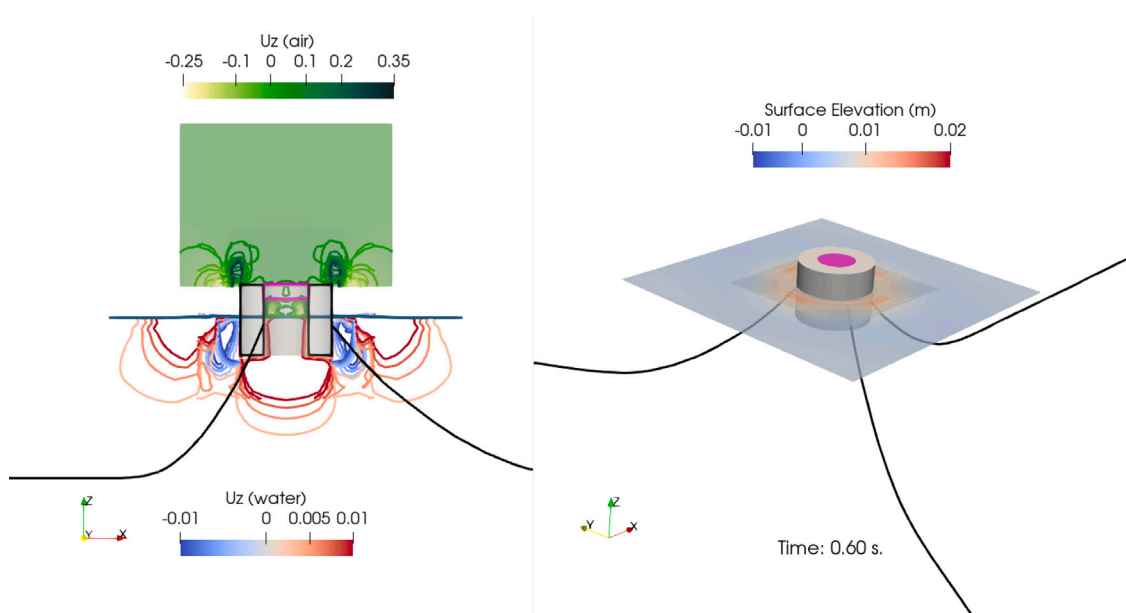


Fig. C.19. Decay of a moored WEC with PTO (Porosity = 0.5). Left panel, side view of the velocity contour lines for water (blue-red) and air (light green-dark green); right panel, top view of surface elevation on the free surface (VoF = 0.5).

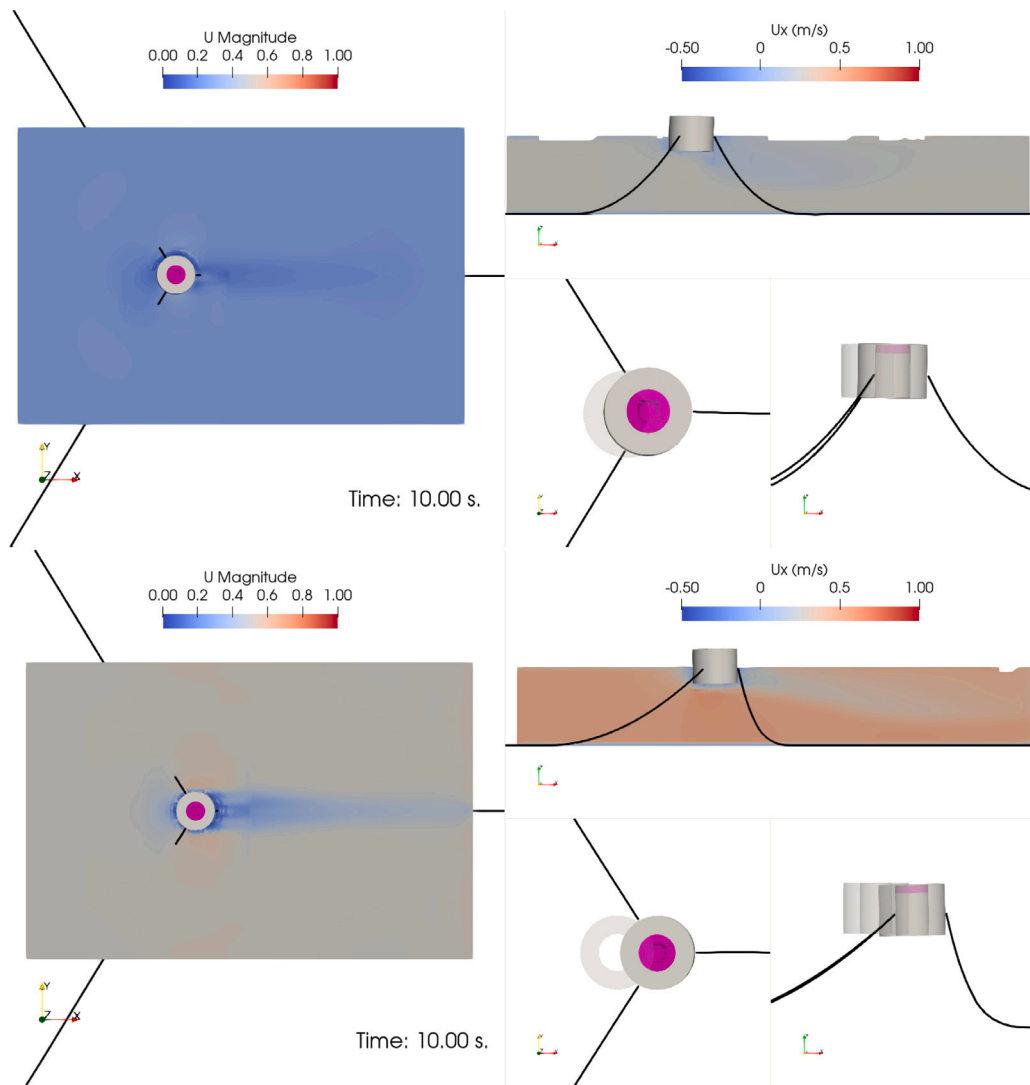


Fig. D.20. WEC displacement under constant current (first row $U_c = 0.25$ m/s, second row, $U_c = 0.50$ m/s) with PTO (porosity = 0.50). Left panel (velocity magnitude on plane XY, $Z = 0.8$ m), top-right panel (velocity in the span-wise direction, plane XZ, $Y = 0$ m), bottom-right panels (top view of the WEC, plane XY, and side view of the WEC, plane XZ).

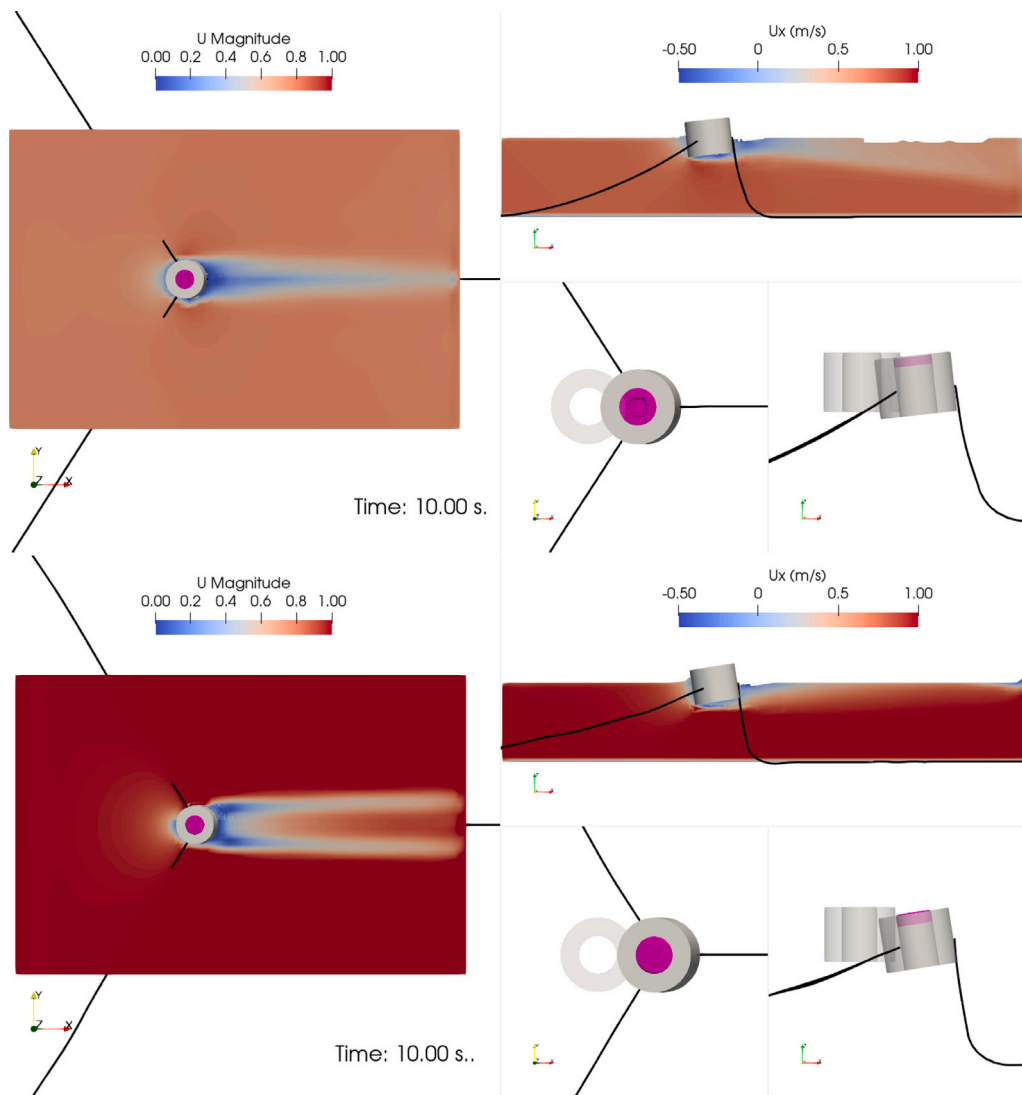


Fig. D.21. WEC displacement under constant current (first row $U_c = 0.75$ m/s, second row, $U_c = 1.0$ m/s) with PTO (porosity = 0.50). Left panel (velocity magnitude on plane XY, $Z = 0.8$ m), top-right panel (velocity in the span-wise direction, plane XZ, $Y = 0$ m), bottom-right panels (top view of the WEC, plane XY, and side view of the WEC, plane XZ).

The second part of this work is related to numerically prove that the PTO damping can be modelled as a porous medium. Three different tests are performed to demonstrate the capability of the numerical model. First, a series of free decay tests are performed varying levels of PTO damping. It is observable that the different characterisations of the PTO have very little influence in the response of the moored WEC in a decay test (when it is released from a given excitation in surge $\delta = 0.114$ m). Then, currents are used to highlight the capability of the model to reproduce large displacements. For a WEC with PTO under constant currents, it can be seen that when increasing the current magnitude, the displacement of the WEC is as well amplified. For very big values, a hydraulic jump is created behind the structure, inducing nonlinear interactions with the floating body. Again, the different characterisations of the PTO have very little influence. Finally, the interaction with regular waves are used to highlight that numerical simulations are complementary to experimental campaigns. It can be seen that different characterisations of the PTO have influence in the main displacements of the floating body.

As future work, it would be interesting to analyse other frictional forces exerted to the air by different modelisations of the complex structure of a PTO, a part from Van Gent (1995). For future research it is also important to extend and further validate the compressibility of the air, as for design purposes it is very important to properly represent the air flow through the PTO.

CRediT authorship contribution statement

Gabriel Barajas: Writing – review & editing, Writing – original draft, Visualization, Software, Methodology, Formal analysis, Data curation, Conceptualization. **Javier L. Lara:** Writing – review & editing, Supervision, Project administration, Funding acquisition, Conceptualization. **Josh Davidson:** Writing – review & editing, Methodology, Formal analysis, Conceptualization. **Alessandro Romano:** Writing – review & editing, Writing – original draft, Methodology, Investigation, Data curation, Conceptualization.

Declaration of competing interest

The authors declare that they have no known competing financial interests or personal relationships that could have appeared to influence the work reported in this paper.

Acknowledgments

Josh Davidson is funded by MCIN and by the European Union NextGenerationEU/PRTR-C17.I1, as well as by IKUR Strategy under the collaboration agreement between Ikerbasque Foundation and BCAM on behalf of the Department of Education of the Basque Government.

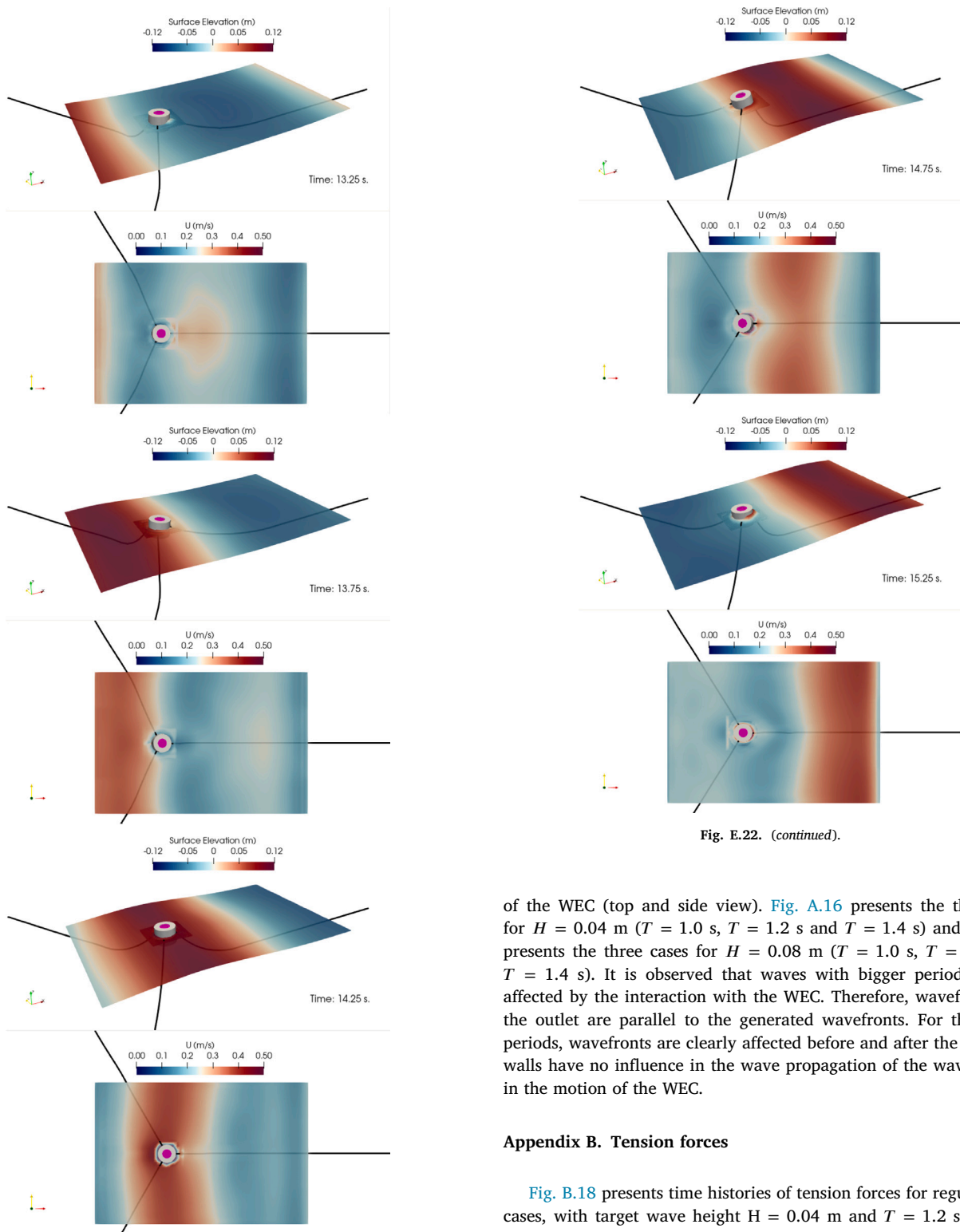


Fig. E.22. (continued).

Fig. E.22. Upper panel, 3D view of surface elevation on the free surface (VoF = 0.5). Bottom panel, 2D view of the velocity magnitude on the plane XY ($z = 0.8$ m). Time $t = (13.25$ s, 13.75 s, 14.25 s, 14.75 s and 15.25 s), respectively. 5th order Stokes regular waves, $H = 0.2$ m, $T = 3.0$ s.

Appendix A. Regular waves interaction with a moored wec

Figs. A.16 and A.17 depict the surface elevation (m) and the velocity magnitude (m/s) on the free surface (VoF = 0.5) and the displacement

of the WEC (top and side view). Fig. A.16 presents the three cases for $H = 0.04$ m ($T = 1.0$ s, $T = 1.2$ s and $T = 1.4$ s) and Fig. A.17 presents the three cases for $H = 0.08$ m ($T = 1.0$ s, $T = 1.2$ s and $T = 1.4$ s). It is observed that waves with bigger periods are less affected by the interaction with the WEC. Therefore, wavefronts near the outlet are parallel to the generated wavefronts. For the smaller periods, wavefronts are clearly affected before and after the WEC. The walls have no influence in the wave propagation of the wavefronts or in the motion of the WEC.

Appendix B. Tension forces

Fig. B.18 presents time histories of tension forces for regular waves cases, with target wave height $H = 0.04$ m and $T = 1.2$ s and $H = 0.08$ m and $T = 1.2$ s. Present work (blue line), numerical (dashed black line) and experimental (black dots) by Palm et al. (2016).

Appendix C. Free decay test of moored WEC with PTO

Fig. C.19 shows a side view (left panel) of the velocity contour lines for water (blue-red) and air (light green-dark green) and a top view (left pane) of the surface elevation (in meters) on the free surface (VoF = 0.5) generated by the free decay test ($n = 0.5$). It can be seen that velocity air is damped when passing through the PTO.

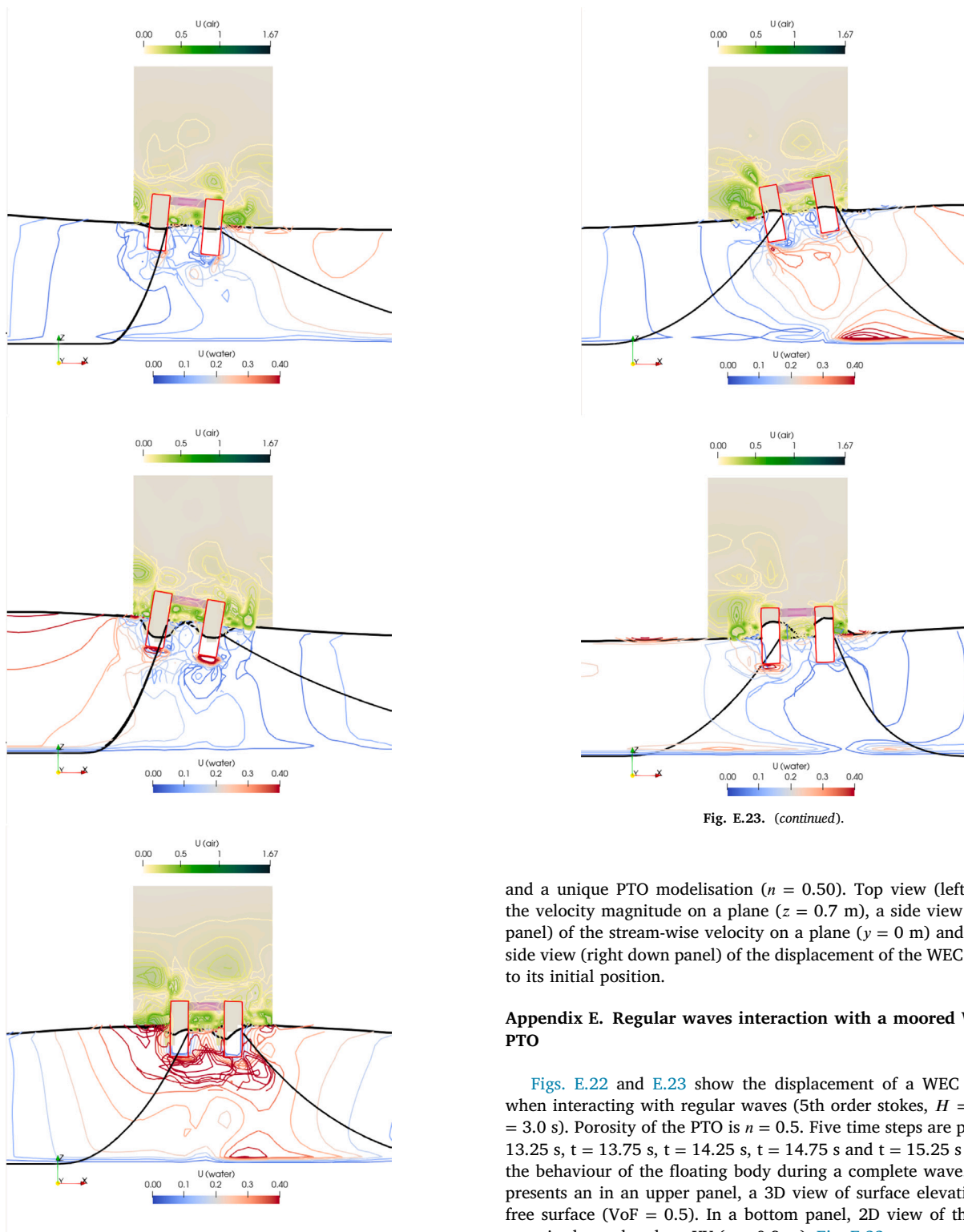


Fig. E.23. (continued).

Fig. E.23. Side view of the velocity contour lines for water (blue-red) and air (light green-dark green). Time $t = (13.25 \text{ s}, 13.75 \text{ s}, 14.25 \text{ s}, 14.75 \text{ s} \text{ and } 15.25 \text{ s})$, respectively. 5th order Stokes regular waves, $H = 0.2 \text{ m}$, $T = 3.0 \text{ s}$.

Appendix D. Input current test of moored WEC with PTO

Figs. D.20 and D.21 shows the final displacement ($t = 10 \text{ s}$), when a constant current interacts with a moored floating WEC with a modelised PTO, for four different currents ($U_c = [0,25, 0,50, 0,75, 1,00]$)

and a unique PTO modelisation ($n = 0.50$). Top view (left panel) of the velocity magnitude on a plane ($z = 0.7 \text{ m}$), a side view (right top panel) of the stream-wise velocity on a plane ($y = 0 \text{ m}$) and a top and side view (right down panel) of the displacement of the WEC compared to its initial position.

Appendix E. Regular waves interaction with a moored WEC with PTO

Figs. E.22 and E.23 show the displacement of a WEC with PTO when interacting with regular waves (5th order Stokes, $H = 0.2 \text{ m}$, $T = 3.0 \text{ s}$). Porosity of the PTO is $n = 0.5$. Five time steps are plotted, $t = 13.25 \text{ s}$, $t = 13.75 \text{ s}$, $t = 14.25 \text{ s}$, $t = 14.75 \text{ s}$ and $t = 15.25 \text{ s}$ to present the behaviour of the floating body during a complete wave. Fig. E.22 presents an in an upper panel, a 3D view of surface elevation on the free surface ($\text{VoF} = 0.5$). In a bottom panel, 2D view of the velocity magnitude on the plane XY ($z = 0.8 \text{ m}$). Fig. E.23 presents a side view of the velocity contour lines for water (blue-red) and air (light green-dark green). As in the decay test, it can be seen the air trapped inside the chamber. The high nonlinear phenomenon of wave sloshing and air compressibility (that is neglected in the numerical model), might have an important role in the overall pneumatic performance.

References

Çelik, A., Altunkaynak, A., 2020. Determination of hydrodynamic parameters of a fixed owc by performing experimental and numerical free decay tests. Ocean Eng. 204, 106827.

- Chen, H., Hall, M., 2022. Cfd simulation of floating body motion with mooring dynamics: Coupling moordyn with openfoam. *Appl. Ocean Res.* 124, 103210.
- Chen, H., Medina, T.A., Cercos-Pita, J.L., 2024. Cfd simulation of multiple moored floating structures using openfoam: An open-access mooring restraints library. *Ocean Eng.* 303, 117697.
- Chowdhury, O.R., Kim, H.g., Park, D.g., Cho, Y., Shin, C., Park, J., 2015. Development of a simple and innovative wave energy harvester suitable for ocean sensor network application. *Int. J. Smart Home* 9, 197–210.
- Constant, E., Favier, J., Meldi, M., Meliga, P., Serre, E., 2017. An immersed boundary method in openfoam: verification and validation. *Comput. & Fluids* 157, 55–72.
- Crema, I., Simonetti, I., Cappietti, L., Oumeraci, H., 2015. Laboratory experiments on oscillating water column wave energy converters integrated in a very large floating structure. In: *Proceedings of the 11th European Wave and Tidal Energy Conference, Nantes, France*. pp. 6–11.
- Davidson, J., Karimov, M., Szelechman, A., Windt, C., Ringwood, J., 2019. Dynamic mesh motion in openfoam for wave energy converter simulation. In: *14th OpenFOAM Workshop*.
- Davidson, J., Ringwood, J.V., 2017. Mathematical modelling of mooring systems for wave energy converters—a review. *Energies* 10, 666.
- de Oliveira Costa, D., Fernandes, A.C., Junior, J.S.S., 2023. Optimization of system of oscillating water columns to mitigate pitch response of fpso platforms submitted to head waves. *Ocean Eng.* 286, 115729.
- Di Paolo, B., Lara, J.L., Barajas, G., Losada, J.J., 2021a. Wave and structure interaction using multi-domain couplings for Navier–Stokes solvers in openfoam®. Part I: Implementation and validation. *Coast. Eng.* 164, 103799.
- Di Paolo, B., Lara, J.L., Barajas, G., Losada, J.J., 2021b. Waves and structure interaction using multi-domain couplings for Navier–Stokes solvers in openfoam®. Part II: Validation and application to complex cases. *Coast. Eng.* 164, 103818.
- Didier, E., Paixão Conde, P., 2011. Numerical simulation of an oscillating water column wave energy converter with and without damping.
- Didier, E., Teixeira, P.R., 2024. Numerical analysis of 3d hydrodynamics and performance of an array of oscillating water column wave energy converters integrated into a vertical breakwater. *Renew. Energy* 225, 120297.
- Dong, Y., Tan, W., Chen, H., Yuan, J., 2024. Numerical modeling of wave interaction with a porous floating structure consisting of uniform spheres. *Phys. Fluids* 36, 087133.
- Du, X., Zhang, M., Kang, H., Chang, H., Yu, H., 2021. Theoretical study on a novel piezoelectric ocean wave energy harvester driven by oscillating water column. *Energy Sources A* 1–21.
- ESI-Group, 2021. *Openfoam the open source cfd toolbox*. URL: <https://www.openfoam.com/>.
- Falcão, A.F., Henriques, J.C., 2016. Oscillating-water-column wave energy converters and air turbines: A review. *Renew. Energy* 85, 1391–1424.
- Falcão, A.F., Henriques, J.C., Gomes, R.P., Portillo, J.C., 2022. Theoretically based correction to model test results of owc wave energy converters to account for air compressibility effect. *Renew. Energy* 198, 41–50.
- Gadelho, J., Guedes Soares, C., Barajas, G., Lara, J.L., 2022. Cfd analysis of the pto damping on the performance of an onshore dual chamber owc. *Trends Marit. Technol. Eng.* 381–389.
- Guanche, R., Losada, I.J., Lara, J.L., 2009. Numerical analysis of wave loads for coastal structure stability. *Coast. Eng.* 56, 543–558.
- Gubesch, E., Abdussamie, N., Penesis, I., Chin, C., 2022. Effects of mooring configurations on the hydrodynamic performance of a floating offshore oscillating water column wave energy converter. *Renew. Sustain. Energy Rev.* 166, 112643.
- Gurnari, L., Filianoti, P.G., Camporeale, S.M., 2022. Fluid dynamics inside a u-shaped oscillating water column (owc): 1d vs. 2d cfd model. *Renew. Energy* 193, 687–705.
- Gurnari, L., Filianoti, P.G., Torresi, M., Camporeale, S.M., 2020. The wave-to-wire energy conversion process for a fixed u-owc device. *Energies* 13, 283.
- Güths, A., Teixeira, P., Didier, E., 2022. A novel geometry of an onshore oscillating water column wave energy converter. *Renew. Energy* 201, 938–949.
- Henriques, J., Portillo, J.C., Gato, L., Gomes, R., Ferreira, D., Falcão, A., 2016. Design of oscillating-water-column wave energy converters with an application to self-powered sensor buoys. *Energy* 112, 852–867.
- Higuera, P., Lara, J.L., Losada, I.J., 2013. Realistic wave generation and active wave absorption for Navier–Stokes models: Application to openfoam®. *Coast. Eng.* 71, 102–118.
- Higuera, P., Lara, J.L., Losada, I.J., 2014. Three-dimensional interaction of waves and porous coastal structures using OpenFOAM®. Part I: formulation and validation. *Coast. Eng.* 83, 243–258.
- Howe, D., 2020. *Integration of Oscillating Water Column Wave Energy Converters Within Multi-Use Maritime Structures* (Ph.D. thesis). University of Tasmania.
- Huang, L., Li, Y., Benites-Munoz, D., Windt, C.W., Feichtner, A., Tavakoli, S., Davidson, J., Paredes, R., Quintana, T., Ransley, E., et al., 2022. A review on the modelling of wave-structure interactions based on openfoam. *OpenFOAM® J.* 2, 116–142.
- Iturrioz, A., Guanache, R., Lara, J., Vidal, C., Losada, I., 2015. Validation of openfoam® for oscillating water column three-dimensional modeling. *Ocean Eng.* 107, 222–236.
- Jacobsen, N.G., van Gent Marcel, R., Fredsøe, J., 2017. Numerical modelling of the erosion and deposition of sand inside a filter layer. *Coast. Eng.* 120, 47–63.
- Jasak, H., 1996. *Error Analysis and Estimation for the Finite Volume Method with Applications to Fluid Flows* (Ph.D. thesis). Imperial College London (University of London).
- Kamath, A., Bihs, A., A, Ø.A., 2015a. Numerical modeling of power take-off damping in an oscillating water column device. *Int. J. Mar. Energy* 10, 1–16.
- Kamath, A., Bihs, H., Arntsen, Ø.A., 2015b. Numerical investigations of the hydrodynamics of an oscillating water column device. *Ocean Eng.* 102, 40–50.
- Katsidoniotaki, E., Götteman, M., 2022. Numerical modeling of extreme wave interaction with point-absorber using openfoam. *Ocean Eng.* 245, 110268.
- Khan, M.A., Barajas, G., Gaeta, M.G., Lara, J.L., Archetti, R., 2024. Hydrodynamic analysis and optimization of a floating wave energy converter with moonpool using openfoam. *Appl. Ocean Res.* 142, 103847.
- Korde, U.A., Gish, L.A., Bacelli, G., Coe, R.G., 2024. Wave energy conversion using a small tubular free-floating device. *J. Ocean Eng. Mar. Energy* 10, 57–69.
- Lara, J.L., del Jesus, M., Losada, I.J., 2012. Three-dimensional interaction of waves and porous coastal structures: Part ii: Experimental validation. *Coast. Eng.* 64, 26–46.
- Lara, J.L., Losada, I.J., Maza, M., Guanache, R., 2011. Breaking solitary wave evolution over a porous underwater step. *Coast. Eng.* 58, 837–850.
- Larsen, B.E., Fuhrman, D.R., 2018. On the over-production of turbulence beneath surface waves in Reynolds-averaged Navier–Stokes models. *J. Fluid Mech.* 853, 419–460.
- Lin, P., 1998. *Numerical Modeling of Breaking Waves*. Cornell University.
- Liu, P.L.F., Wu, T.R., Raichlen, F., Synolakis, C.E., Borrero, J.C., 2005. Runup and rundown generated by three-dimensional sliding masses. *J. Fluid Mech.* 536, 107–144.
- Losada, I.J., Lara, J.L., del Jesus, M., 2016. Modeling the interaction of water waves with porous coastal structures. *J. Waterw. Port Coast. Ocean Eng.* 142, 03116003.
- Masoomi, M., Sarlak, H., Rezanejad, K., 2023. Hydrodynamic performance analysis of a new hybrid wave energy converter system using openfoam. *Energy* 269, 126807.
- Masuda, Y., An experience of wave power generator through tests and improvement. In: *Evans, D.V., de Falcão, A.F.O. (Eds.), Hydrodynamics of Ocean Wave-Energy Utilization*. Springer, Berlin Heidelberg, pp. 445–452.
- Mathias, N., Marini, R.N., Morais, T., Luís, M., Rosa-Santos, P., 2021. Response of a self-powered offshore floating support structure with an owc for powering a lidar device. *Ocean Eng.* 220, 108366.
- Medina-Lopez, E., Moñino, R.J., Clavero, M., Ortega-Sanchez, M., 2019. Oscillating water column performance under the influence of storm development. *Energy* 166, 765–774.
- Moñino, A., Medina-López, E., Clavero, M., Benslimane, S., 2017. Numerical simulation of a simple owc problem for turbine performance. *Int. J. Mar. Energy* 20, 17–32.
- M'zoughi, F., Aboutalebi, P., Garrido, I., Garrido, A.J., De La Sen, M., 2021. Complementary airflow control of oscillating water columns for floating offshore wind turbine stabilization. *Mathematics* 9, 1364.
- Oikonomou, C.L., Gomes, R.P., Gato, L.M., 2021. Unveiling the potential of using a spar-buoy oscillating-water-column wave energy converter for low-power stand-alone applications. *Appl. Energy* 292, 116835.
- Opoku, F., Uddin, M., Atkinson, M., 2023. A review of computational methods for studying oscillating water columns—the Navier–Stokes based equation approach. *Renew. Sustain. Energy Rev.* 174, 113124.
- Palm, J., Eskilsson, C., 2022. Facilitating large-amplitude motions of wave energy converters in openfoam by a modified mesh morphing approach. *Int. Mar. Energy J.* 5, 257–264.
- Palm, J., Eskilsson, C., Bergdahl, L., 2017. An hp-adaptive discontinuous Galerkin method for modelling snap loads in mooring cables. *Ocean Eng.* 144, 266–276.
- Palm, J., Eskilsson, C., Paredes, G.M., Bergdahl, L., 2016. Coupled mooring analysis for floating wave energy converters using cfd: Formulation and validation. *Int. J. Mar. Energy* 16, 83–99.
- Paredes, G.M., Palm, J., Eskilsson, C., Bergdahl, L., Taveira-Pinto, F., 2016. Experimental investigation of mooring configurations for wave energy converters. *Int. J. Mar. Energy* 15, 56–67.
- Pinguet, R., Benoit, M., Molin, B., Rezende, F., 2022. Cfd analysis of added mass, damping and induced flow of isolated and cylinder-mounted heave plates at various submergence depths using an overset mesh method. *J. Fluids Struct.* 109, 103442.
- Roache, P., 1997. Quantification of uncertainty in computational fluid dynamics. *Ann. Rev. Fluid Mech.* 29, 123–160.
- Romano, A., Lara, J.L., Barajas, G., Di Paolo, B., Bellotti, G., Di Risio, M., Losada, I.J., Girolamo, P.De., 2020. Tsunamis generated by submerged landslides: Numerical analysis of the near-field wave characteristics. *J. Geophys. Res.: Oceans* 125, e2020JC016157.
- Sarmento, A., 1992. Wave flume experiments on two-dimensional oscillating water column wave energy devices. *Exp. Fluids* 12, 286–292.
- Scarpetta, F., Gurnari, L., Torresi, M., Filianoti, P., Camporeale, S., 2017. A cfd simulation of a full-scale u-owc breakwater. In: *Proceedings of the 12th European Wave and Tidal Energy Conference (EWTEC)*, Cork, Ireland.
- Simonetti, I., Cappietti, L., Elsafti, H., Oumeraci, H., 2017. Optimization of the geometry and the turbine induced damping for fixed detached and asymmetric owc devices: A numerical study. *Energy* 139, 1197–1209.
- Stern, F., Wilson, R., Coleman, H., Paterson, E., 2001. Comprehensive approach to verification and validation of cfd simulations—part 1: Methodology and procedures. *J. Fluids Eng.* 123, 793–802.

- Tan, J., Polinder, H., Laguna, A.J., Miedema, S., 2022. A numerical study on the performance of the point absorber wave energy converter integrated with an adjustable draft system. *Ocean Eng.* 254, 111347.
- Van Gent, M.R.A., 1995. *Wave Interaction with Permeable Coastal Structures* (Ph.D thesis). Delft University.
- Viviano, A., Naty, S., Foti, E., 2018. Scale effects in physical modelling of a generalized owc. *Ocean Eng.* 162, 248–258.
- Vukčević, V., 2016. *Numerical Modelling of Coupled Potential and Viscous Flow for Marine Applications* (Ph.D. thesis). University of Zagreb.
- Wang, C., Zhang, Y., 2021. Numerical investigation on the wave power extraction for a 3d dual-chamber oscillating water column system composed of two closely connected circular sub-units. *Appl. Energy* 295, 117009.
- Weber, J., 2012. Wec technology readiness and performance matrix-finding the best research technology development trajectory. In: *Proceedings of the 4th International Conference on Ocean Energy*, Dublin, Ireland.
- Windt, C., Davidson, J., Ringwood, J.V., 2018. High-fidelity numerical modelling of ocean wave energy systems: A review of computational fluid dynamics-based numerical wave tanks. *Renew. Sustain. Energy Rev.* 93, 610–630.
- Xu, C., Huang, Z., 2019. Three-dimensional cfd simulation of a circular owc with a nonlinear power-takeoff: Model validation and a discussion on resonant sloshing inside the pneumatic chamber. *Ocean Eng.* 176, 184–198.
- Zabala, I., Henriques, J., Blanco, J., Gomez, A., Gato, L., Bidaguren, I., Falcão, A., Amezaga, A., Gomes, R., 2019. Wave-induced real-fluid effects in marine energy converters: Review and application to owc devices. *Renew. Sustain. Energy Rev.* 111, 535–549.
- Zhou, Y., Chen, L., Zhao, J., Liu, X., Ye, X., Wang, F., Adcock, T.A., Ning, D., 2023. Power and dynamic performance of a floating multi-functional platform: An experimental study. *Energy* 285, 129367.
- Zhou, Y., Ning, D., Chen, L., Iglesias, G., 2021a. Nonlinear hydrodynamic modeling of an offshore stationary multi-oscillating water column platform. *Ocean Eng.* 227, 108919.
- Zhou, Y., Ning, D., Chen, L., Iglesias, G., 2021b. Nonlinear hydrodynamic modeling of an offshore stationary multi-oscillating water column platform. *Ocean Eng.* 227, 108919.
- Zhou, Y., Ning, D., Liang, D., Cai, S., 2021c. Nonlinear hydrodynamic analysis of an offshore oscillating water column wave energy converter. *Renew. Sustain. Energy Rev.* 145, 111086.
- Zhu, H., Hu, C., Sueyoshi, M., Yoshida, S., 2020. Integration of a semisubmersible floating wind turbine and wave energy converters: an experimental study on motion reduction. *J. Mar. Sci. Technol.* 25, 667–674.